KLOE Note 178
April 2002

Measurement of BR($\phi \rightarrow \pi^0\pi^0\gamma$) with 2000 Data

S. Giovannella, S. Miscetti

INFN - Laboratori Nazionali di Frascati

Abstract

In this note we report the measurement of the branching ratio for the decay $\phi \rightarrow \pi^0\pi^0\gamma$ performed using a 16 pb^{-1} sample of e^+e^- collisions collected at the ϕ-resonance peak. In a model independent way, we determined this branching ratio to be: BR($\phi \rightarrow \pi^0\pi^0\gamma$) = $(\,1.09 \pm 0.03_{\rm stat} \pm 0.05_{\rm syst}\,) \cdot 10^{-4}$. Integrating the two pion invariant mass in the region dominated by the $f_0(980)$ meson, above 700 MeV, we get: BR($\phi \rightarrow \pi^0\pi^0\gamma$) = $(\,0.96 \pm 0.02_{\rm stat} \pm 0.05_{\rm syst}\,) \cdot 10^{-4}$.

1 Introduction

The observation of $\phi \rightarrow \pi^0\pi^0\gamma$ dates 1998 [1] and up to now only two experiments have studied this decay [2, 3]. The interest in a precise measurement of this channel comes from the interpretation of the radiative transition being dominated by the process $\phi \rightarrow f_0(980)\,\gamma$ and from the high value of the BR if the f_0 is a standard $q\overline{q}$ state. A wealth of literature exists on this scalar particle and several models have been proposed to explain its nature: ordinary $q\overline{q}$ meson, $q\overline{q}q\overline{q}$ state, $K\overline{K}$ molecule [4, 5, 6]. The purely neutral decay $\phi \rightarrow \pi^0\pi^0\gamma$ can contribute to clarify the theoretical situation since both the BR and the resonance mass shape depend on the f_0 models, while not suffering of large interference effects as in the $\phi \rightarrow \pi^+\pi^-\gamma$ case [7].

In our experiment, the search for this decay and the development and refinement of the analysis technique have been carried out for at least three years [8, 9]. In this note we avoid to explain all the details concerning the kinematic fit procedure; interested readers can find a complete explanation of this item in Ref. [9]. Furthermore, the analysis cuts have been tuned to obtain a similar analysis efficiency for the processes $\phi \rightarrow f_0\gamma \rightarrow \pi^0\pi^0\gamma$ and $\phi \rightarrow \rho\pi^0 \rightarrow \pi^0\pi^0\gamma$ and are therefore slightly different from the previous report. In this paper we concentrate only on the final measurement of the BR and on the evaluation of the systematic errors. In a forthcoming note [10] we also address the fit procedure developed to extract the contribution of the different processes from the mass distribution.

The note is organized in three main sections: in Sec. 2 we explain in more detailed the reconstruction of prompt photons, in Sec. 3 we evaluate the losses and the systematic errors connected to the pre-selection of the sample while in the last one we report the new analsis cuts, the final evaluation of the systematic errors and the BR measurement.

2 Reconstruction of prompt photons

Since this analysis is based on calorimetry, a more detailed description of the clustering algorithm is given. Using the timing (t) and energy (e) information collected on each cell and its geometrical location, the space hits ($\vec{r}$, t, e) are built. The calorimeter reconstruction builds objects called preclusters by joining contiguous hits in the transverse plane. For each precluster the total energy (E) is obtained summing the energy of the collected hits while the centroids of the space points ($\vec{R}$) and of the timing (T) are calculated as energy weighted averages of the information of the joined cells. A breaker procedure uses the r.m.s of the timing at the edges to separate preclusters composed by two particles impinging along the fibers on the same transversal region. A cluster is then formed by merging the preclusters having $|\Delta R| < 40$ cm and $\Delta T < 2.5$ ns, being R the distance between the average interaction point and the clusters centroid. A theshold of 3 MeV is then applied.

Comparing data and Montecarlo (MC) samples of $e^+e^- \rightarrow \gamma\gamma$ we observe a large discrepancy in the counting of shower fragments (splitted clusters) with $E < 80$ MeV and $\Delta R < 70$ cm [11]. After hardening the merging procedure by joining clusters with $\Delta R < 1.5\ \mathrm{cm}/\sqrt{\mathrm{E\,(GeV)}}$ and $\Delta \mathrm{T} < 3.5$ ns a better agreement is found.

The cluster reconstruction efficiency, $\varepsilon_{\mathrm{clu}}$, is measured using two different control samples: $e^+e^- \rightarrow e^+e^-\gamma$ and $e^+e^- \rightarrow \rho\pi$. This efficiency is 90% at 20 MeV, reaching 100% above 70 MeV. The simulation slightly overestimates $\varepsilon_{\mathrm{clu}}$; this is corrected by adding a description of the energy response in the Montecarlo.

The timing scale is set using $\gamma\gamma$ events with an average precision of few tens of ps. A residual dependence of the timing along the fiber coordinates, up to 300 ps, is still observed due to the timing walk on pulse-height. An ad-hoc correction reduces this effect below 100 ps. A prompt photon is then defined as a neutral particle, *i.e.* a cluster without any close track extrapolation, satisfying the prompt time window requirement of $|T - R/c| < \mathrm{MIN}(5\,\sigma_T, 2\,\mathrm{ns})$.

The presence of accidental clusters due to machine background is controlled looking at out-of-time particles. In the used sample we have measured a rate per event of spurious background clusters of: $(87 \pm 13)\%$ [12]. These accidentals show a soft spectrum and are peaked at small polar angles (θ). The usage of the prompt time window alone reduces this contamination to below 1.8%. Due to the high level of background contamination ($\sim 8\%$ in time window) the QCAL detector was not used in this analysis, thus forcing us to exclude the region with $\theta < 21^\circ$. A description of the machine background is anyhow implemented in the MC by adding to the EMC generated hits the accidental ones collected in the out-of-time window in the data [13].

3 Trigger and data streaming losses

As in all KLOE analysis, the starting sample of the events belonging to the neutral radiative stream (NR) survived the three common pre-selections of the trigger (TRG) [14], the Filfo background rejection (FLF) [15] and the Event Classification algorithm (ECL) [16]. The losses due to these selections have been studied on both data and MC.

The Montecarlo sample consists of 100 000 $\phi \to f_0\gamma \to \pi^0\pi^0\gamma$ events of the official 2001 production [17], where a common reconstruction path is used for all the generated samples. The data reconstruction path for the NR events has instead two specific features: the Filfo filter is inhibited and a specific algorithm is run to partially recover events with a wrong T_0 assignement[1]. As a consequence, the MC events have been reconstructed anew to pass the same algorithms used on data.

The pre-selection efficiencies are then evaluated at the end of the old analysis cuts [9] and are reported in Tab. 1. Since the biggest loss is due to ECL, a complete re-streaming of end 2000 data (runs $15174 \div 17330$) has been performed, applying a very loose filter (NRLOOSE) on the events selected by Filfo. The NRLOOSE procedure select events with

[1] In prompt neutral events the T_0 finder procedure fails only 0.3% of the time because of accidentals. However this effect is not negligible in both data and MC since it is dominated by merging of clusters.

	Efficiency
TRG	$(99.20 \pm 0.06)\%$
FLF	$(99.90 \pm 0.02)\%$
ECL	$(90.4 \pm 0.2)\%$

Table 1: MC efficiencies for trigger, Filfo and Event Classification after analysis cuts.

at least three prompt photons requiring:

1. at least three EMC clusters with $E_\gamma > 7$ MeV in time window;
2. an angular acceptance $|\cos\theta| < 0.951$;
3. total energy of the clusters (including out-of-time ones): $E_{\text{tot}} > 600$ MeV.

Losses due to this selection are expected to be completely negligible from MC. In the re-streaming we have considered only the runs having the luminosity evaluated from VLAB [18]. The whole statistics (Sample A) corresponds to an integrated luminosity of $L_{\text{int}} = (16.0 \pm 0.3)$ pb^{-1}. A sub-sample of these runs ($17280 \div 17330$, $L_{\text{int}} = (979 \pm 1)$ nb^{-1}) have been also filtered and analyzed starting from raw data (Sample B).

3.1 Trigger losses

The KLOE trigger exploits both calorimeter and chamber information. In this analysis we used only the calorimeter trigger which requires at least two fired sectors (LET) with energy above a given threshold (50 MeV for barrel, 150 MeV for endcaps); a cosmic ray veto (CV) then rejects the events with at least two cosmic sectors above 30 MeV. The first analysis requirement is therefore that all the $\phi \to \pi^0\pi^0\gamma$ candidates have to be triggered by the calorimeter. Looking at MC the trigger losses are completely due to the cosmic veto.

In order to check the trigger efficiency, we have first performed a data–MC comparison of the LET trigger distributions. In Figs. 1, 2, 3 the multiplicity of the fired LET is reported for the three calorimeter subdetectors while in Fig. 4 the LET trigger pattern is shown. Since the fired pattern is dominated by triple coincidences and an excellent data–MC agreement is found, we consider negligible the loss due to the LET trigger.

To estimate the effect due to the cosmic veto we used both data and MC. In Montecarlo we expect a loss of $\varepsilon_{\rm cv}(\mathrm{MC}) = (0.80 \pm 0.06)\%$. Since in the streamed data the vetoed events are retained with a prescaling factor of 50 (a factor 5 from DAQ times a factor 10 from reconstruction), the number of expected cosmic veto events in Sample A is given by:

$$N_{\rm cv} = \varepsilon_{\rm cv}(\mathrm{MC}) \cdot N_{\rm ev} = 0.8\% \cdot \frac{2270}{50} = 0.36 \pm 0.03. \quad (1)$$

Looking at the fired bits in the data we have found 1 event due to CV, which corresponds to a poissonian probability P(0.36,1) of 25%. Anyhow, we cannot use this measurement to assign a significative error to this efficiency; for this reason we have estimated an error measuring the losses of CV on $\phi \to \eta\gamma \to 3\gamma/\ 7\gamma$ samples ($\eta3$, $\eta7$). We measure [11] :

$$\left.\begin{array}{l} \varepsilon_{\rm cv} = 6.1 \pm 1.4 \cdot 10^{-3}\ (\eta3) \\ \varepsilon_{\rm cv} = 1.9 \pm 0.8 \cdot 10^{-3}\ (\eta7) \end{array}\right\}\text{data} \quad (2)$$

and

$$\left.\begin{array}{l} \varepsilon_{\rm cv} = 12.2 \pm 0.3 \cdot 10^{-3}\ (\eta3) \\ \varepsilon_{\rm cv} = \ \ 4.3 \pm 0.3 \cdot 10^{-3}\ (\eta7) \end{array}\right\}\text{MC} \quad (3)$$

While the difference of the average values of the loss between $\eta3$ and $\eta7$ samples is explained by the harder energy spectra of $\eta3$, a consistent correction factor $R = \varepsilon_{\rm cv}(\mathrm{MC})/\varepsilon_{\rm cv}(\mathrm{data})$ is obtained from the two samples ($R = 2.06 \pm 0.44$). This data–MC discrepancy can be ascribed to the non perfect MC description of the shower profiles. Correcting of R the MC efficiency for the $\phi \to \pi^0\pi^0\gamma$ sample we get: $\varepsilon_{\rm cv}(\mathrm{data}) = (3.9 \pm 0.8) \cdot 10^{-3}$.

3.2 Filfo losses

The Filfo behaviour is checked by looking at the analysis output for runs which are common to both Sample A and Sample B. In Sample A, 150 $\phi \to \pi^0\pi^0\gamma$ candidates are found, yielding to a number of expected rejected events of:

$$N_{\rm filt} = \varepsilon_{\rm loss}(\mathrm{MC}) \cdot N_{\rm ev} = 0.1\% \cdot 150 = 0.15. \quad (4)$$

The same 150 events are found in Sample B, thus showing no data–MC discrepancy with this statistics. The systematic error on Filfo losses, evaluated directly from data, can be only bound to be less than 2% @ 95% C.L. We consider this loss and the related error negligible in the following.

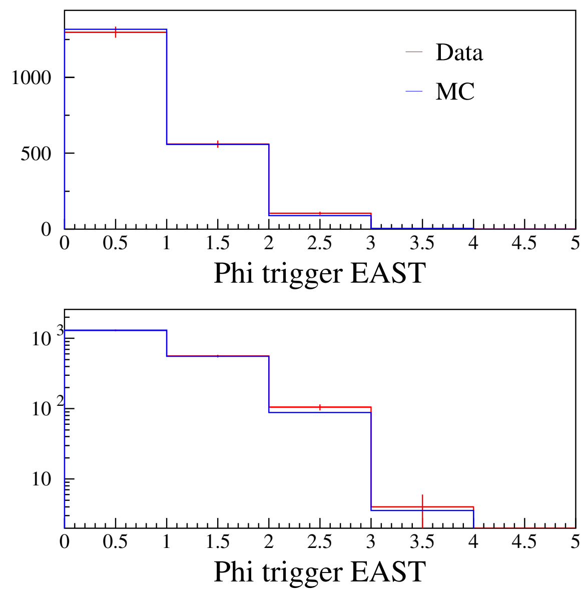

Figure 1: Number of fired LET trigger sector for EndCap East. Data–MC comparison is shown in both linear (top) and logarithmic (bottom) scale.

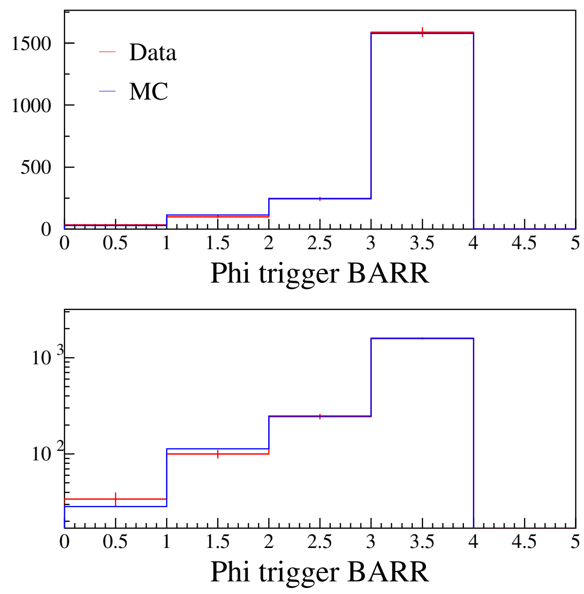

Figure 2: Number of fired LET trigger sector for Barrel. Data–MC comparison is shown in both linear (top) and logarithmic (bottom) scale.

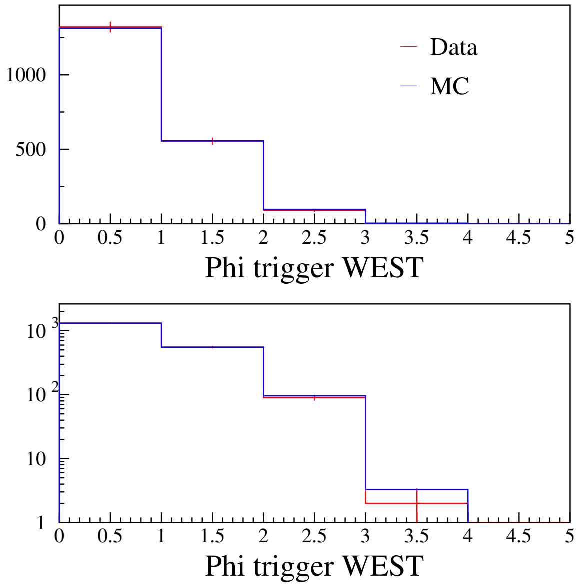

Figure 3: Number of fired LET trigger sector for EndCap West. Data–MC comparison is shown in both linear (top) and logarithmic (bottom) scale.

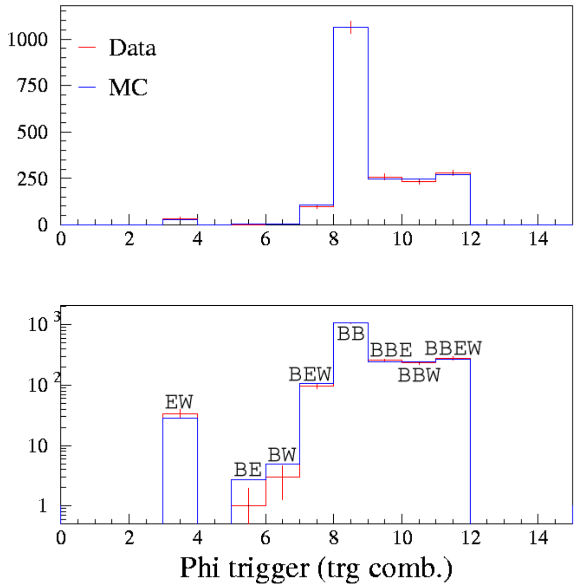

Figure 4: Data–MC comparison: LET trigger pattern in both linear (top) and logarithmic (bottom) scale. The pattern reported indicates the coincidences of fired sectors in endcap East (E), barrel (B) and endcap West (W) subdetectors.

	MC	Data
Cut 1	0.1%	5.6%
Cut 2	9.1%	8.6%
Cut 3	0.2%	0.6%
OTHERS	0.2%	4.3%
Total	9.6%	18.5%

Table 2: Losses due to ECL for data and MC events after all analysis cuts applied.

3.3 Event classification losses

In order to evaluate the losses due to ECL, the corresponding algorithm is applied on both re-streamed data (Sample A) and $\phi \to f_0\gamma \to \pi^0\pi^0\gamma$ MC events. This algorithm is based on the three following requirements:

1. there are no tracks in the event;
2. there is at least one cluster with ($E > E_{\rm max} = 280$ MeV and $\beta > 0.85$) or the condition $\langle\beta\rangle > 0.95$ is satisfied for events having more than 7 prompt clusters. $\beta = R/Tc$ is the reconstructed speed of the cluster while $\langle\beta\rangle$ is the energy weighted average of β over all clusters.
3. $E_{\rm tot} > 700$ MeV and $P_{\rm tot} < 200$ MeV$/c$, where $E_{\rm tot}$ and $P_{\rm tot}$ are the total energy and momentum of the EMC clusters, including the out-of-time ones.

The inefficiency due to ECL, $\eta_{\rm ECL}$, is defined as the ratio between the events rejected by ECL and the final $\phi \to \pi^0\pi^0\gamma$ candidates, and is reported in Tab. 2 as a function of the different requirements both for data and MC. In this table, we refer as OTHERS to the losses having apparently no explanation and that do not satisfy the three cuts listed above.

In the MC, the inefficiency is dominated by Cut 2. Indeed, this cut could be critical for the $\phi \to f_0\gamma \to \pi^0\pi^0\gamma$ analysis since:

1. the ECL efficiency shows a strong f_0 mass dependence: a $\sim 20\%$ variation is observed over the whole mass range ($300 \div 1020$ MeV) allowed to this decay;

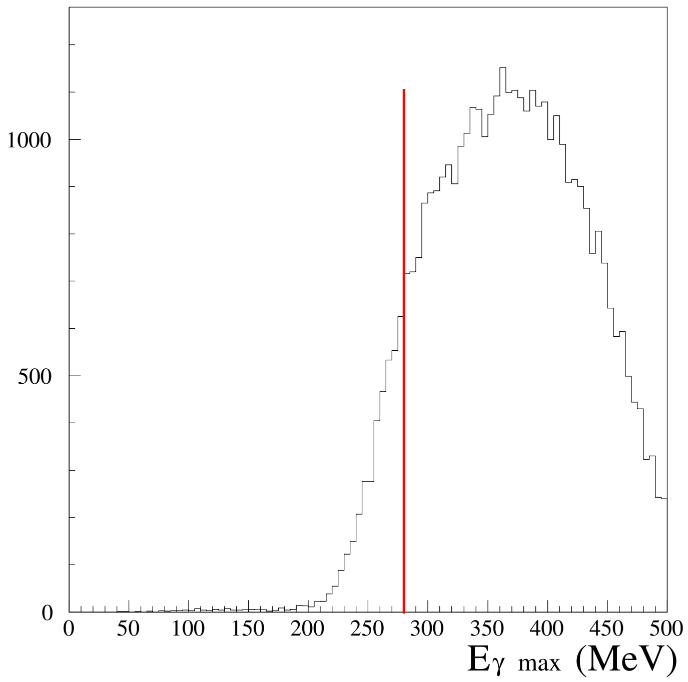

Figure 5: Maximum energy of the photons for $\phi \to f_0\gamma \to \pi^0\pi^0\gamma$ MC events. The red line shows the cut of the neutral radiative algorithm.

2. the energy threshold used ($E_{\rm max}$) is well contained in the distribution of the maximum photon energy in the event (see Fig. 5) and the ECL efficiency can suffer of a not proper calorimeter and energy scale calibration (which anyhow was the usual running condition for 2000 data streaming).

However, Cut 2 is well described by MC and there is not a large discrepancy with the value found in the data. Still, the overall losses in the data is twice the MC one. Half of this discrepancy is accounted for by Cut 1, since there are a lot of events contamineted by short spiralizing tracks near the beam pipe due to accidental overlap of machine background (see Fig. 6). The remaining difference is due to a typo in the T_0 search algorithm,[2] which created the OTHERS loss for data.

[2]This has been corrected in the re–streaming of 2001 data.

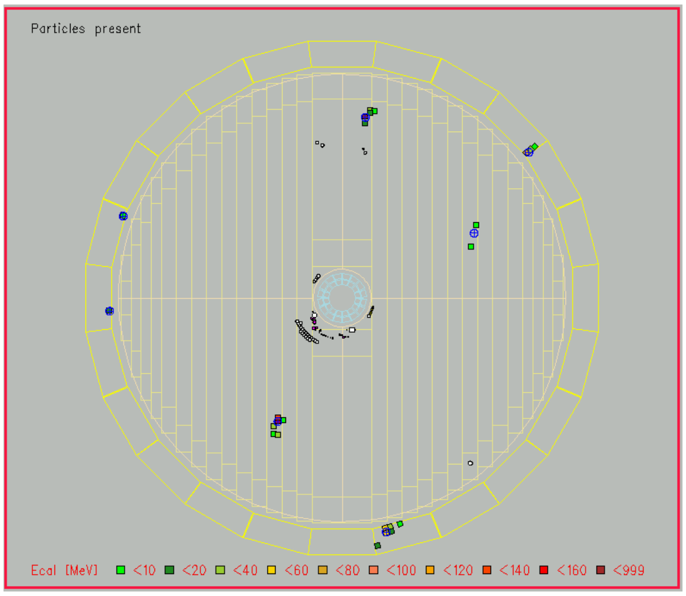

Figure 6: A $\phi \to \pi^0\pi^0\gamma$ candidate from 2000 KLOE data (run 16124, event 737110). This events is rejected from the event classification because of the small track near the interaction point, due to machine background.

4 Events selection and BR measurement of $\phi \to \pi^0\pi^0\gamma$

For the reasons explained in the previous section we use Sample A, instead of the output of NR filter, for the final counting of events. We also assume negligible the systematic error due to this preselection since its efficiency is very high and the data have been properly calibrated. Furthermore, the analysis of the $\phi \to \pi^0\pi^0\gamma$ is changed with respect to the last one [9] in few relevant points:

1. the lower cutoff at 700 MeV on the reconstructed $\pi^0\pi^0$ invariant mass ($M_{\pi\pi}$) has been removed thus allowing to study the mass shape in the whole kinematic region;

2. two amplitudes can contribute to $\phi \to \pi^0\pi^0\gamma$:

   - $\phi \to S\gamma$ with $S \to \pi^0\pi^0$ ($S\gamma$), where S is a scalar meson (as the f_0)
   - $\phi \to \rho\pi^0$ with $\rho \to \pi^0\gamma$ ($\rho\pi$).

Since they interfere, the incoherent subtraction of the $\rho\pi$ background is not performed anymore;

3. the analysis cuts have been tuned to get the same efficiency for both $S\gamma$ and $\rho\pi$ processes. The two contributions are then disentangled by applying a fit to the $M_{\pi\pi}$ spectrum [10].

4.1 Selection of the starting sample

The background channels to the decay $\phi \to \pi^0\pi^0\gamma$ ($\pi\pi\gamma$) are:

1. the non resonant $e^+e^- \to \omega\pi^0 \to \pi^0\pi^0\gamma$ process ($\omega\pi$);
2. $\phi \to \eta\pi^0\gamma$, with $\eta \to \gamma\gamma$ ($\eta\pi\gamma$);
3. $\phi \to \eta\gamma \to \pi^0\pi^0\pi^0\gamma$ ($\eta\gamma$) that mimics the signal whenever two of the photons are lost or merged;
4. $\phi \to K_S K_L$;
5. $e^+e^- \to \gamma\gamma(\gamma)$ and $\phi \to \eta\gamma/\pi^0\gamma \to \gamma\gamma\gamma$ with spurious clusters due to splitting or in-time machine background.

A preliminar selection of the $\pi^0\pi^0\gamma$ final state retains events which have 5 prompt photons with $E \geq 7$ MeV and $\theta \geq \theta_{\rm min} = 23°$. Of the 124 575 events surviving this preselection, the background due to $\phi \to K_S K_L$ is reduced to a negligible amount after requiring that the total energy ($E_{\rm tot}$) and total momentum ($\vec{P}_{\rm tot}$) of the prompt photons satisfy: $E_{\rm tot} > 800$ MeV and $|\vec{P}_{\rm tot}| < 200$ MeV/c. The contamination due to $e^+e^- \to \gamma\gamma$ events with in-time accidental clusters is cleaned by rejecting events with $175° < |\phi_1 - \phi_2| < 185°$ and $(E_1 + E_2) > 900$ MeV, where $\phi_{1,2}$ and $E_{1,2}$ are the azimuthal angles and energies of the two most energetic clusters. After these cuts the sample is reduced to 15 825 events.

On the surviving events a kinematic fit (Fit1) based on the energy-momentum conservation at the interaction point is applied, improving the energy resolution down to 3%. Photons are then paired into π^0's by searching for the best combination which minimizes a selection χ^2 ($\chi^2_{\rm sel}$) in both $\pi\pi\gamma$ and $\omega\pi$ hypotheses. In this last case, the $\pi^0\gamma$ invariant mass ($M_{\pi\gamma}$) is also required to be consistent with the ω mass, M_ω. More explicitely the

Channel	S/B	Efficiency	Rejection factor	Expected events
$e^+e^- \to \omega\pi^0 \to \pi^0\pi^0\gamma$	0.80	4.6%	8.7	339 ± 24
$\phi \to \eta\pi^0\gamma \to 5\gamma$'s	3.52	9.9%	4.0	166 ± 16
$\phi \to \eta\gamma \to \pi^0\pi^0\pi^0\gamma$	0.027	6.8×10^{-4}	5.9×10^3	159 ± 12

Table 3: Background channels for $\phi \to \pi^0\pi^0\gamma$.

$\chi^2_{\rm sel}$ is defined as:

$$\chi^2_{\rm sel} = \sum_{i=1}^{2} \frac{(M^i_{\gamma\gamma} - M_\pi)^2}{\sigma^2_\pi} + \frac{(M_{\pi\gamma} - M_\omega)^2}{\sigma^2_\omega} \tag{5}$$

where M_π is the π^0 mass while $M_{\gamma\gamma}$ and σ_π are the $\gamma\gamma$ invariant mass and its resolution respectively. σ_π and σ_ω are calibrated on both data and MC samples by fitting the $M_{\gamma\gamma}$ distribution.

The correct combination of photons is found by this procedure 89% (96%) of the time for the $\pi\pi\gamma$ ($\omega\pi$) case. The agreement of energy scale and resolution between data and MC is checked by comparing the χ^2, $\chi^2_{\rm sel}$ and invariant mass distributions after Fit1. A further description of this item and of the related systematics can be found in Par. 4.4. A second kinematic fit (Fit2) is then performed, constraining the assigned $\gamma\gamma$ pairs to M_π for both $\pi\pi\gamma$ and $\omega\pi$ hypotheses.

4.2 Evaluation of the $e^+e^- \to \omega\pi^0 \to \pi^0\pi^0\gamma$ background

After the sample selection, the remaining background channels are $\omega\pi$, $\eta\pi\gamma$ and $\eta\gamma$. The rate ratio between signal and background, reported in Tab. 3, is evaluated for these processes using the cross sections measured at KLOE [19, 11].

Since the non resonant $e^+e^- \to \omega\pi^0 \to \pi^0\pi^0\gamma$ process ($\omega\pi$) is the most relevant background in the $\phi \to \pi^0\pi^0\gamma$ ($\pi\pi\gamma$) search and its cross section, $\sigma(\omega\pi)$, varies rapidly in the ϕ resonance region [20], its effective value has to be determined. Similarly, the $\pi\pi\gamma$ decay is the main background in the $\omega\pi$ search. For these reasons an iterative procedure is done to evaluate the relative fraction of these decays, until converging to stable values within the errors. The $\pi\pi\gamma$ simulation assumes a scalar intermediate state with a generated $\pi^0\pi^0$ mass spectrum ($M_{\rm true}$) calibrated with the data itself (see Fig. 28). The generated shape used in the simulation is shown in Fig. 7.

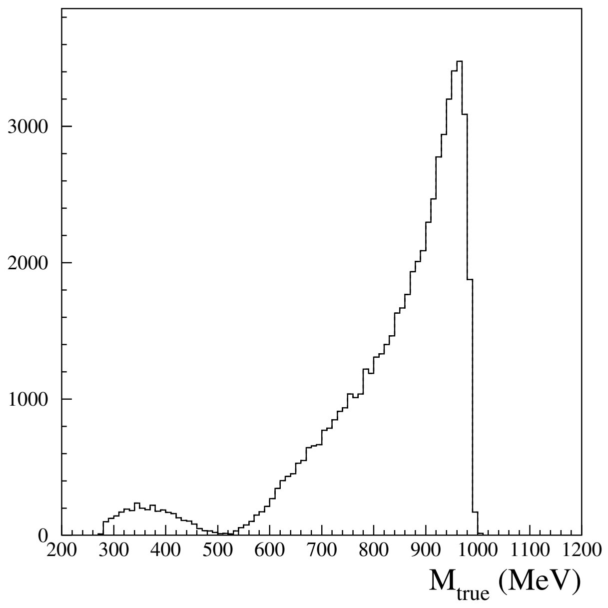

Figure 7: Montecarlo distribution of the f_0 invariant mass.

The evaluation of the $e^+e^- \to \omega\pi^0 \to \pi^0\pi^0\gamma$ cross section is done starting from the events surviving Fit2 on the $\omega\pi$ hypothesis. The candidates should satisfy the further cuts:

1) $\chi^2/\mathrm{ndf} \leq 3$ from Fit2;

2) $\Delta M_{\pi\gamma} = |M_{\pi\gamma} - M_\omega| \leq 3\,\sigma_\omega$ using the output variables of Fit1;

3) $|\cos\psi < 0.8|$ using the output variables of Fit1.

ψ is the angle between the γ and the π^0 in the $\pi^0\pi^0$ rest frame. In Fig. 8 the χ^2/ndf distributions are shown: the data–MC agreement for Fit2 is excellent even at the selection level of 5 prompt photons; the shapes of various distribution using the photon momenta of Fit1 are also checked. The comparison for $\Delta M_{\pi\gamma}/\sigma_\omega$ and $|\cos\psi|$ (Fig. 9) shows a good agreement for the first quantity while a residual discrepancy between data and MC appears at high $|\cos\psi|$ values. This is the reason for Cut 3). Distributions of masses and energies in the data after background subtraction are used as data quality check in Figs. 10 and 11, where the expected shapes for the signals are also overimposed. The data–MC agreement is excellent with the exception of the energies of the ω decay products; such a discrepancy seems to be correlated with the observed discrepancy at high values of $|\cos\psi|$.[3]

Assuming no interference effects in the $M_{\pi\gamma}$ spectra between $\omega\pi$ and $S\gamma$–$\rho\pi^0$ amplitudes and after subtracting the expected background, the final count of events is $N_{\omega\pi} = 2821 \pm 59$. Correcting for the selection efficiency ($\varepsilon_{\omega\pi} = 38.2\%$) we get:

$$\sigma_{\rm eff}(\omega\pi) = \frac{N_{\omega\pi}}{L_{\rm int}\cdot\varepsilon_{\omega\pi}} = (\,0.46 \pm 0.01_{\rm stat} \pm 0.03_{\rm syst}\,)\ {\rm nb} \tag{6}$$

The systematic error is dominated by the data–MC shape discrepancy at $|\cos\psi| > 0.8$ and is evaluated measuring the cross section removing cut 3).

4.3 Selection of the $\phi \to \pi^0\pi^0\gamma$ decay

The selection of the $\pi\pi\gamma$ decay reported in Ref. [9] (OLDANA) has been modified in order to extend the search to the whole $M_{\pi\pi}$ spectrum. Indeed, the behaviour of the OLDANA efficiency for the $S\gamma$ process as a function of $M_{\pi\pi}$ exhibits a fast reduction whenever decreasing the mass. A value of efficiency of $\sim$ 15% is reached for $M_{\rm true} < 600$ MeV (Fig. 12). Moreover, the efficiency behaviour is different between $\rho\pi$ and $S\gamma$ processes, thus complicating the fit procedure to extract their relative contributions. We have tuned the selection procedure in order to reduce these two effects. The new requirements defining the $\phi \to \pi^0\pi^0\gamma$ candidates (NEWANA) are:

1) $\chi^2/{\rm ndf} \leq 3$, using Fit2 in the $\pi\pi\gamma$ hypothesis;

2) $\omega\pi$ veto: rejection of events satisfying $\chi^2_{\omega\pi}/{\rm ndf} \leq 3$ and $\Delta M_{\pi\gamma} \leq 3\,\sigma_\omega$;

3) $\Delta M_{\gamma\gamma} = |M_{\gamma\gamma} - M_\pi| \leq 5\,\sigma_\pi$, using Fit1 output.

The difference with OLDANA consists in removing the cut used to reject the $\rho\pi$ and $\eta\pi\gamma$ backgrounds ($|\cos\psi| > 0.4$, with photons paired in the $\omega\pi$ hypothesis) and in the insertion

[3] A possible explanation of such a discrepancy comes from the simulation used for the process $e^+e^- \to \omega{\pi^0}_1 \to {\pi^0}_2\gamma{\pi^0}_1$. The differential decay rate assumes a simple Breit-Wigner for the ω considering only the $\omega \to {\pi^0}_2\gamma$ decay. No exchange ${\pi^0}_1$–${\pi^0}_2$ term exists in the generator. In the calculation of $e^+e^- \to \rho^0\pi^0 \to \pi^0\pi^0\gamma$ the exchange term considerably counts and creates a double shoulder in the $M_{\pi\pi}$ spectrum [10].

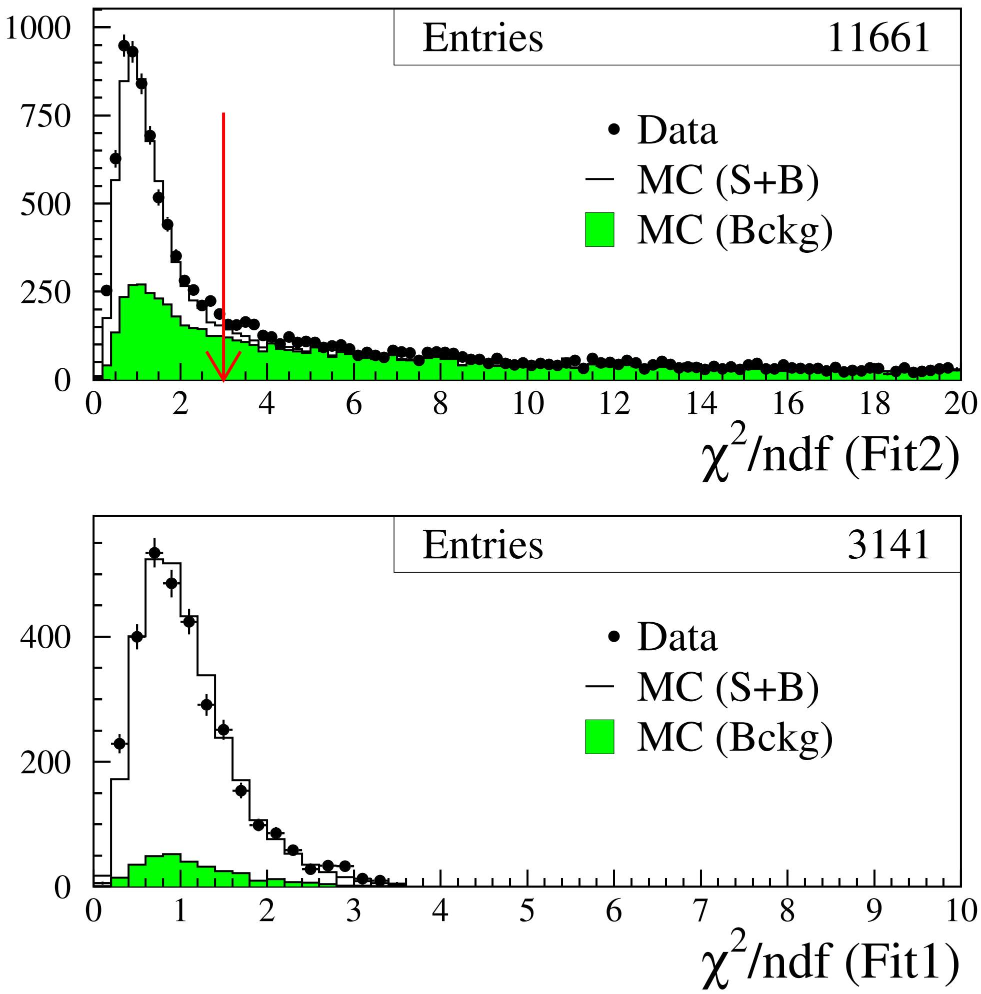

Figure 8: Data–MC comparison for $e^+e^- \to \omega\pi^0 \to \pi^0\pi^0\gamma$ events: χ^2/ndf for Fit2 after selection (top) and for Fit1 after all analysis cuts (bottom). The red arrow shows the χ^2/ndf cut.

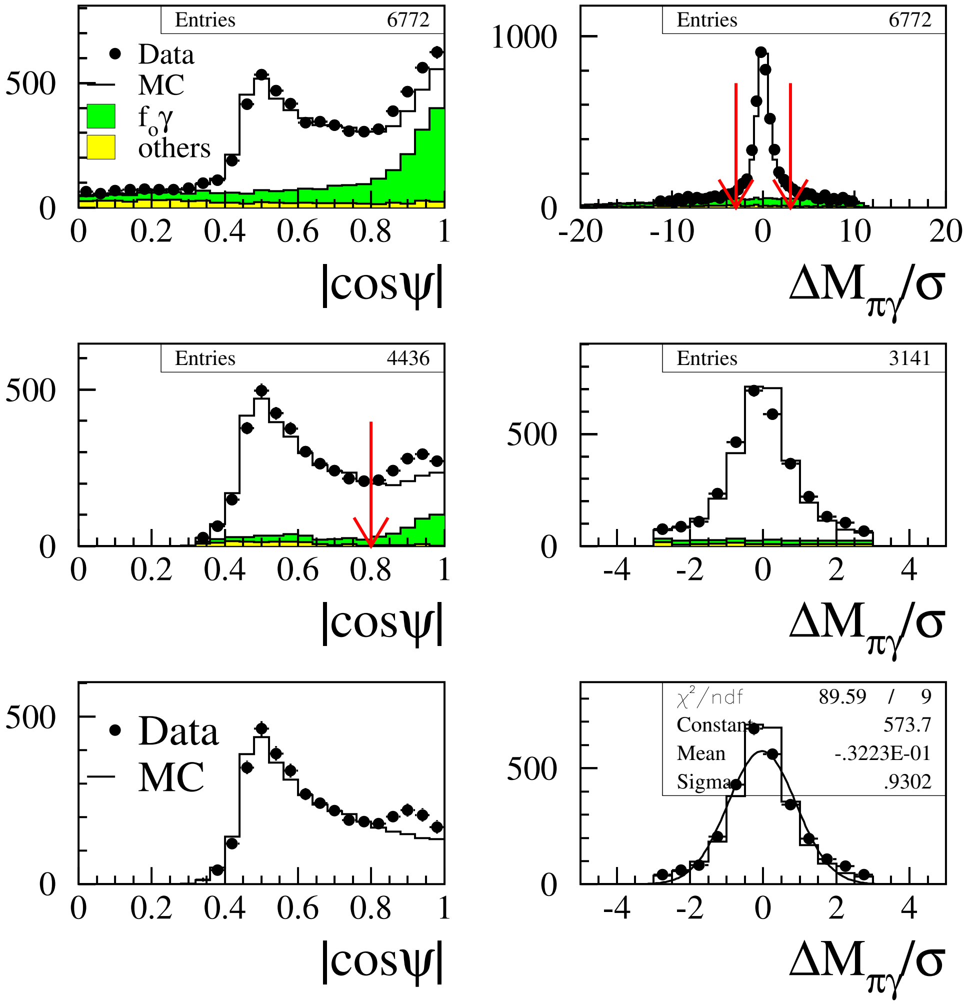

Figure 9: Data–MC comparison for $e^+e^- \to \omega\pi^0 \to \pi^0\pi^0\gamma$ events: $|\cos\psi|$ and normalized $\pi^0\gamma$ invariant mass distributions after χ^2/ndf cut (top) and after all analysis cuts before (middle) and after background subtraction (bottom). For the angular distributions the $|\cos\psi|$ cut is removed to show the data–MC discrepancy at high $|\cos\psi|$ values. The red arrows show the analysis cuts used for the determination of the cross section.

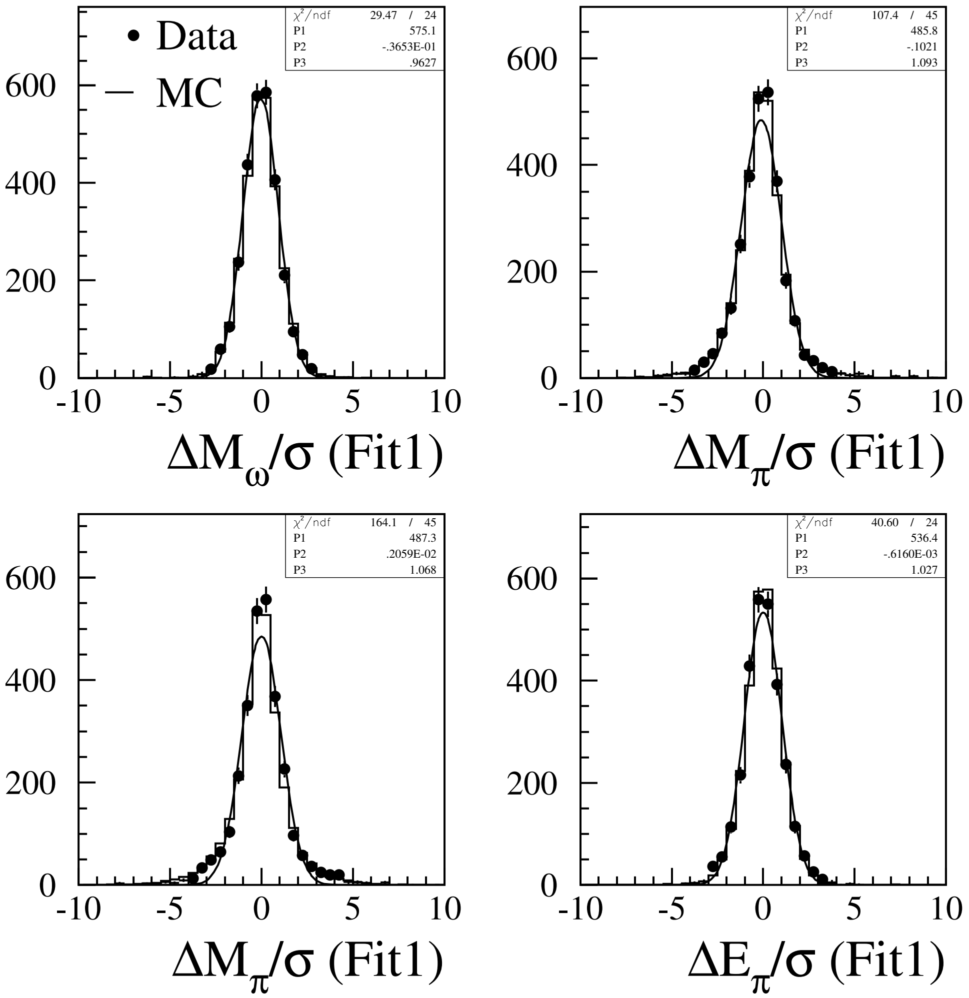

Figure 10: Data–MC comparison for $e^+e^- \to \omega\pi^0 \to \pi^0\pi^0\gamma$ events after background subtraction: normalized masses for ω (top-left) and π^0 (top-right, bottom-left) mesons and normalized energy of the π^0 produced with the ω (bottom-right) after analysis cuts. Output quantities of Fit1 are used.

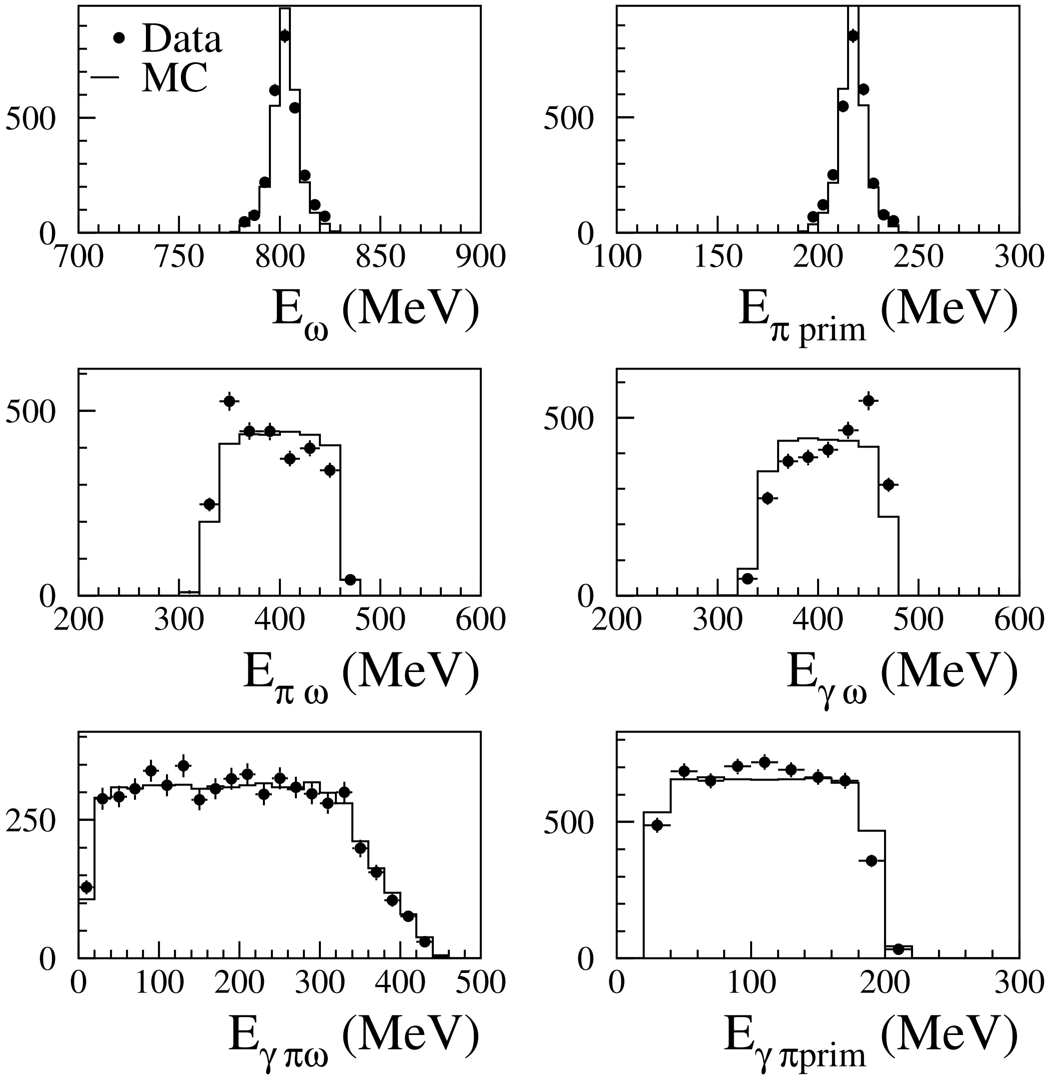

Figure 11: Data–MC comparison for $e^+e^- \to \omega\pi^0 \to \pi^0\pi^0\gamma$ events after background subtraction: energy distributions for mesons and photons of the event after analysis cuts. Output of Fit2 is used. Energy spectrum for ω and π^0 produced in the collision (top), energy spectrum for the π^0 and γ produced in the radiative decay of the ω (middle) and distribution of photon energy spectrum for the γ's coming from the π^0 from ω and from the primary π^0 (bottom).

of cut 3), to further reduce the residual background (see Fig. 14). The NEWANA selection results having an efficiency which is higher than OLDANA for $M_{\rm true} < 800$ MeV and showing no dependence on the intermediate state (Fig. 12). Contributions of the different selection cuts are reported in Fig. 13 as a function of $M_{\rm true}$. The biggest inefficiency comes from the photons selection criteria and it is dominated by the geometrical acceptance; the $\omega\pi$ veto explains the efficiency modulation vs $M_{\rm true}$. Efficiencies and rejection factors for the backgrounds after the whole selection are listed in Tab. 3.

The χ^2/ndf distribution for Fit2 is shown in Fig. 15.top after cuts 2) and 3). An excellent data–Montecarlo agreement is observed in the whole range. A comparison between data and MC for the 3102 events of the final sample is shown in Figs. 15.middle-bottom, 16. After subtracting the expected background events of Tab. 3, the number of $\phi \to \pi^0\pi^0\gamma$ candidates is reduced to 2438 ± 61. The corresponding control distributions are shown in Figs. 17, 18. The overall agreement is excellent; the shape of the angular distributions suggests that the $S\gamma$ intermediate state is the dominant process. Indeed the distribution of $\cos\theta$ for the radiative photons exibhits the correct $(1+\cos^2\theta)$ behaviour while the $\cos\psi$ distribution is flat as expected for a scalar particle. The large errors introduced on the $\pi^0\pi^0$ invariant mass distribution for $M_{\pi\pi} \sim 600$ MeV are due to the data–MC discrepancy of the $e^+e^- \to \omega\pi^0 \to \pi^0\pi^0\gamma$ events, which creates a counting difference in this $M_{\pi\pi}$ region; these errors are conservatively taken as half of the difference in number of events counted using the standard $\omega\pi$ veto or adding the cut $|\cos\psi| < 0.8$.

4.4 Systematics on mass resolution and photon pairing

The output of Fit1 has been used to study the π^0 mass resolution. The sample is divided into five ranges of $E_{\rm min}$, the minimum energy between the two photons forming the π^0. The resulting $M_{\gamma\gamma}$ distributions, reported in Fig. 19, show a good data–MC agreement and have a gaussian shape except in the $E_{\rm min}$ range $(0 \div 50)$ MeV, where the proximity to the reconstruction energy threshold produces some distorsions. The results of the gaussian fit are used to study the behaviour of the mass scale and resolution as a function of $E_{\rm min}$. The difference of the mean value between $M_{\gamma\gamma}$ and the nominal π^0 mass (Fig. 20) shows a drop of 3 MeV in the first point for both data and Montecarlo. The mass resolution, shown in Fig. 21, has a similar behaviour for the two samples, except in the first $E_{\rm min}$ range,

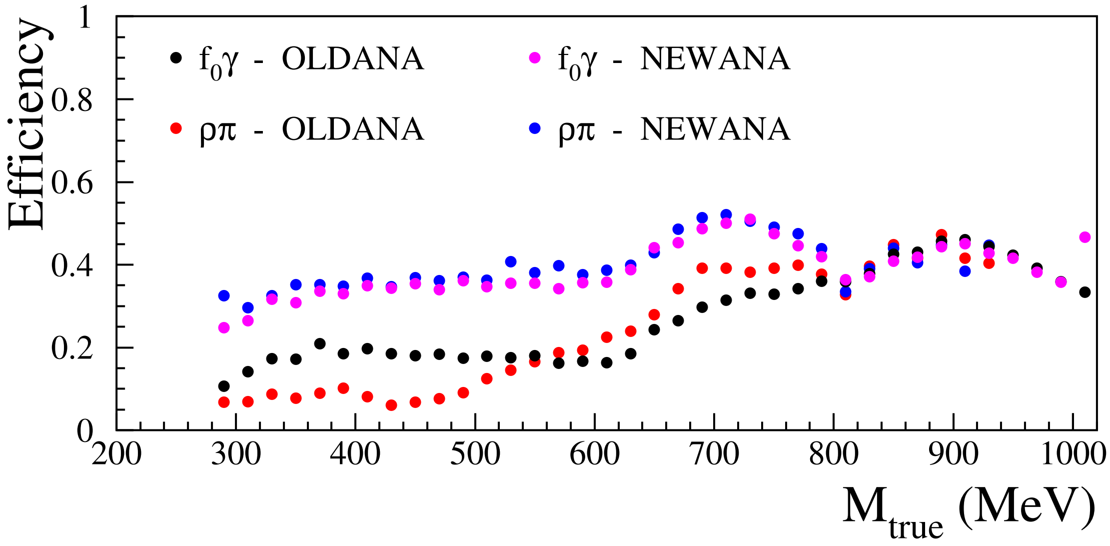

Figure 12: OLDANA–NEWANA comparison of analysis efficiency for $\phi \to f_0\gamma \to \pi^0\pi^0\gamma$ and $\phi \to \rho^0\pi^0 \to \pi^0\pi^0\gamma$ events.

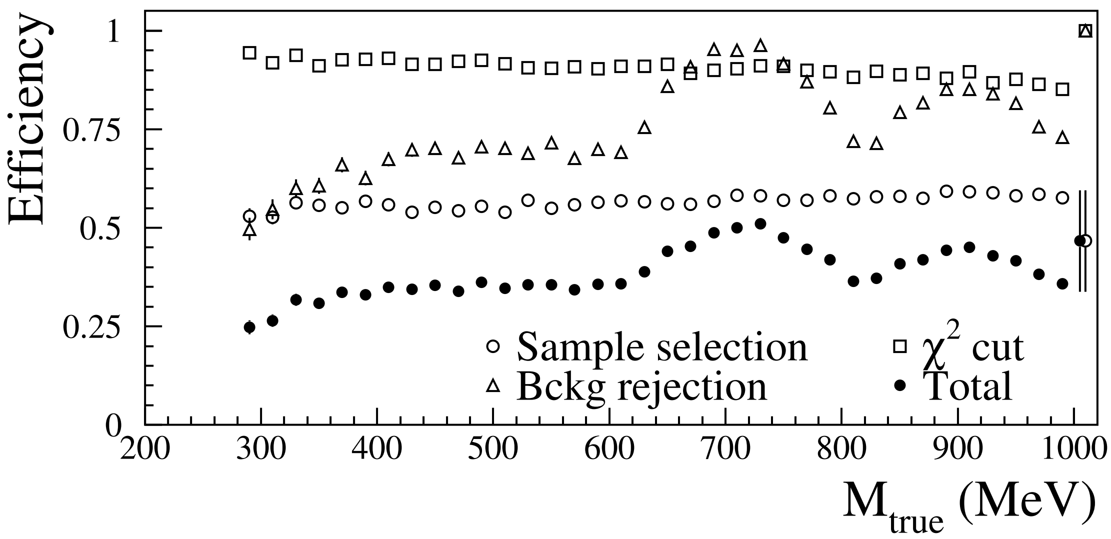

Figure 13: NEWANA analysis efficiency as a function of $M_{\rm true}$ for $\phi \to \pi^0\pi^0\gamma$ events. Contributions of single cuts are also shown: selection of 5 prompt photons ($\circ$), χ^2/ndf (Fit2) cut ($\Box$), selection cuts 2) and 3) ($\triangle$) and overall efficiency ($\bullet$).

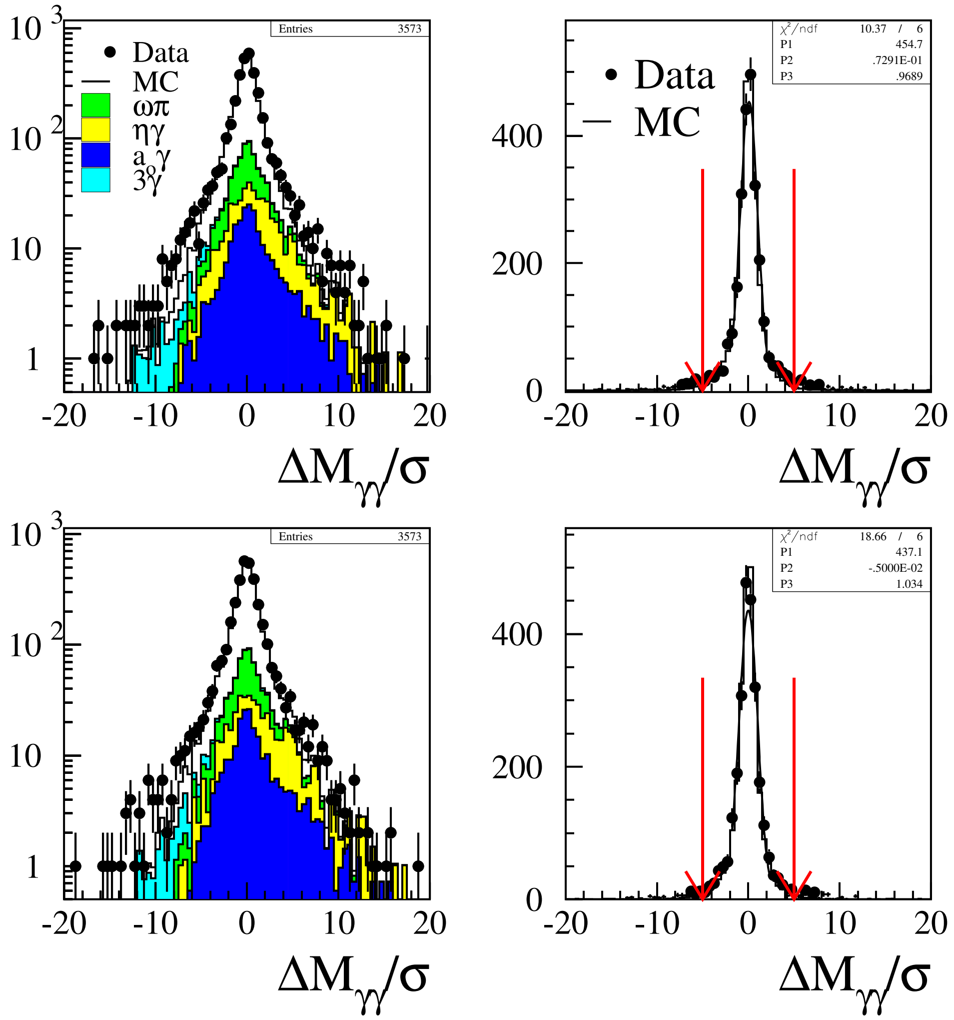

Figure 14: Data–MC comparison for $\phi \to \pi^0\pi^0\gamma$ events after cuts 1) and 2): $\Delta M_{\gamma\gamma}/\sigma_\pi$ distributions of the two π^0 (top and bottom) before (left) and after (right) background subtraction using Fit1 output. The expected background contribution is displayed in colors. The red arrows show the analysis cut to reduce the $\gamma\gamma\gamma$ background.

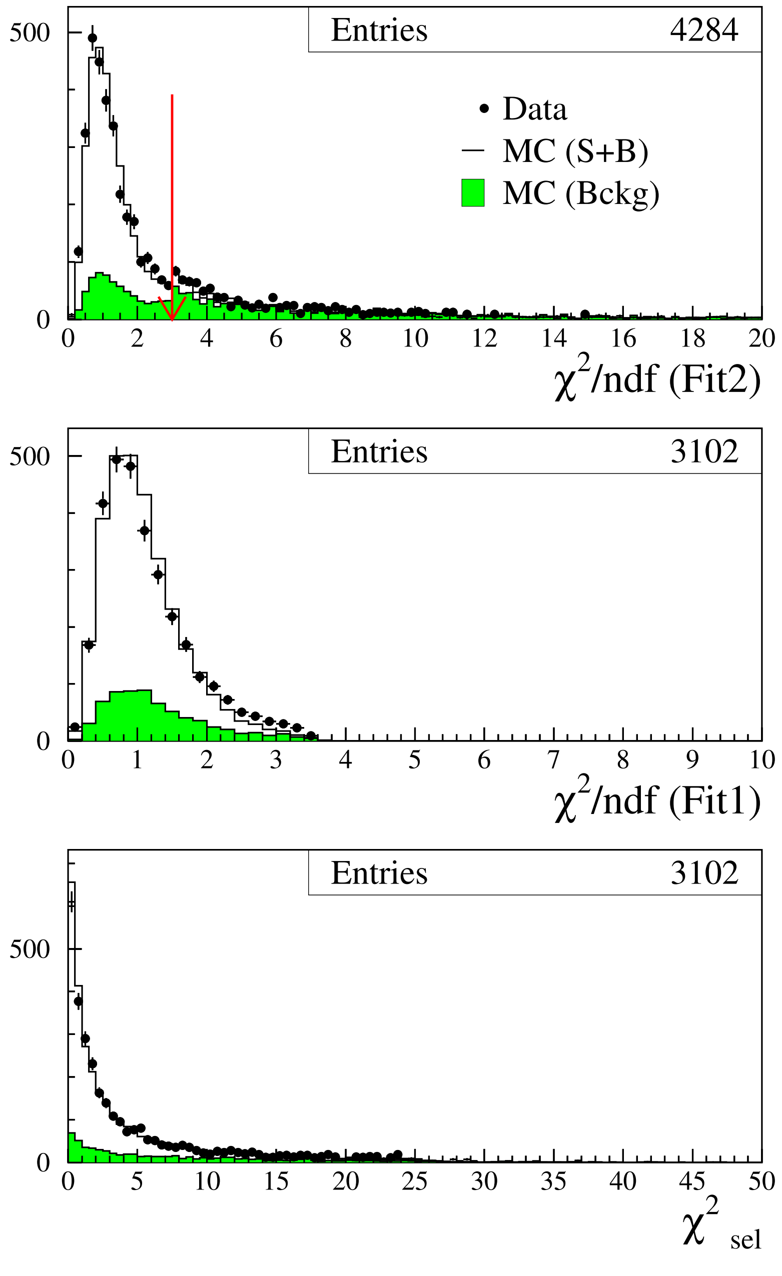

Figure 15: Data–MC comparison for $\phi \to \pi^0\pi^0\gamma$ events: Fit2 χ^2/ndf after cuts 2., 3. (top) and Fit1 χ^2/ndf (middle), $\chi^2_{\rm sel}$ (bottom) after all analysis cuts. The red arrow shows the χ^2/ndf cut.

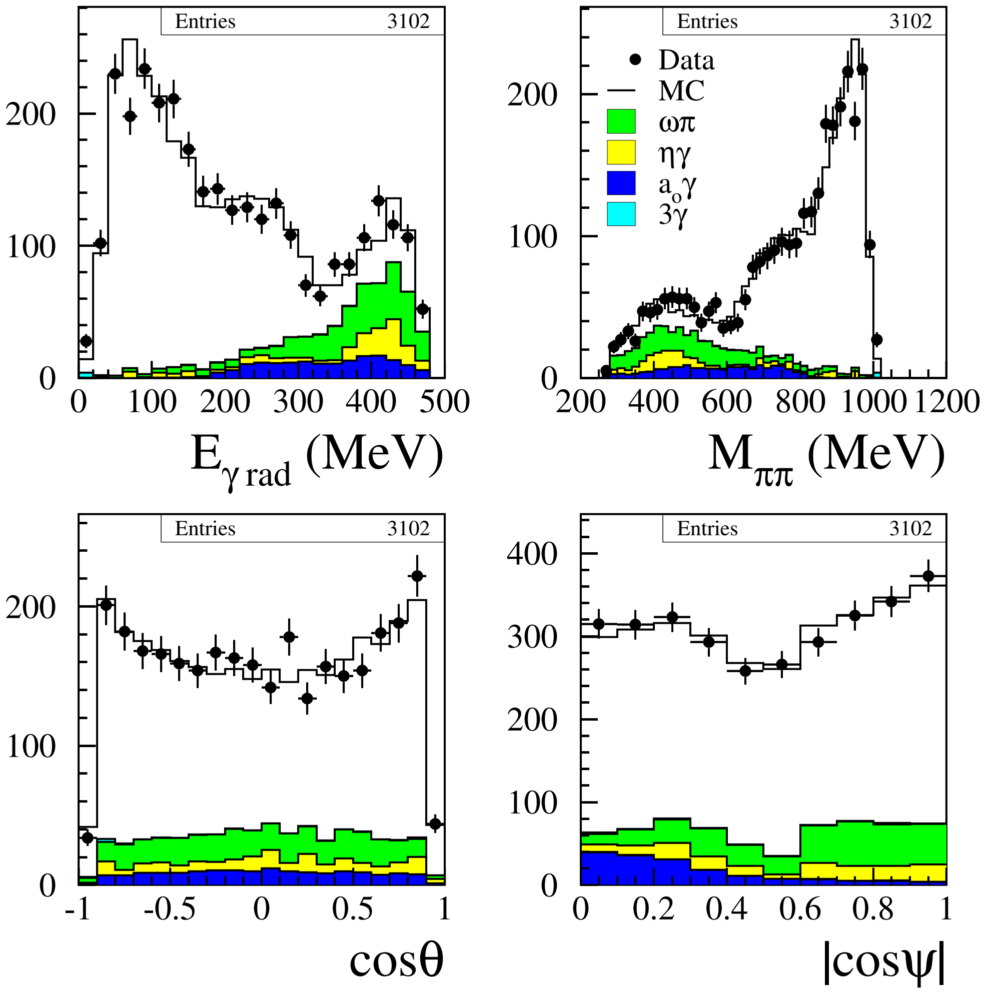

Figure 16: Data–MC comparison for $\phi \to \pi^0\pi^0\gamma$ events: energy of the radiative photon (up-left), $\pi^0\pi^0$ invariant mass (up-right), polar angle (bottom-left) and $|\cos\psi|$ distribution (bottom-right) after analysis cuts. The expected background contribution is displayed in colors. The output of Fit2 is used for all variables.

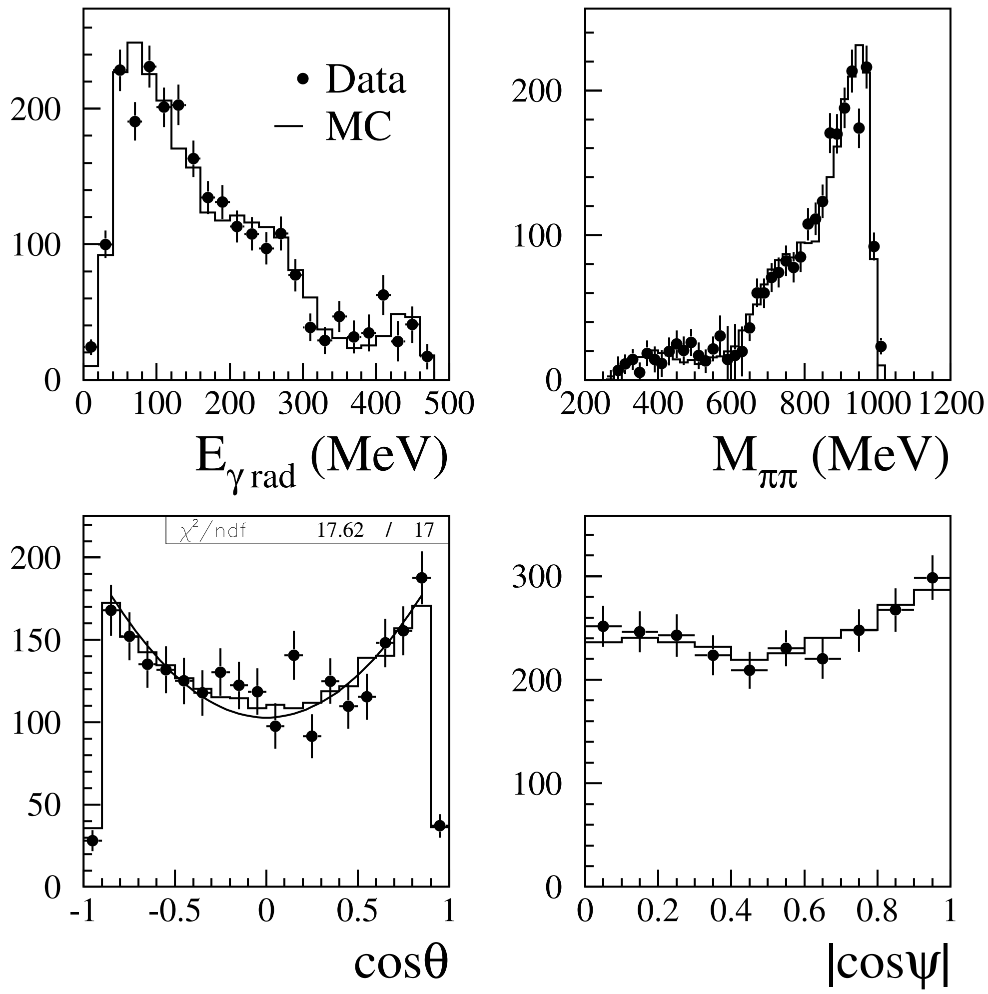

Figure 17: Data–MC comparison for $\phi \to \pi^0\pi^0\gamma$ events after background subtraction: energy of the radiative photon (up-left), $\pi^0\pi^0$ invariant mass (up-right), polar angle (bottom-left) and $|\cos\psi|$ distribution (bottom-right). The output of Fit2 is used for all variables.

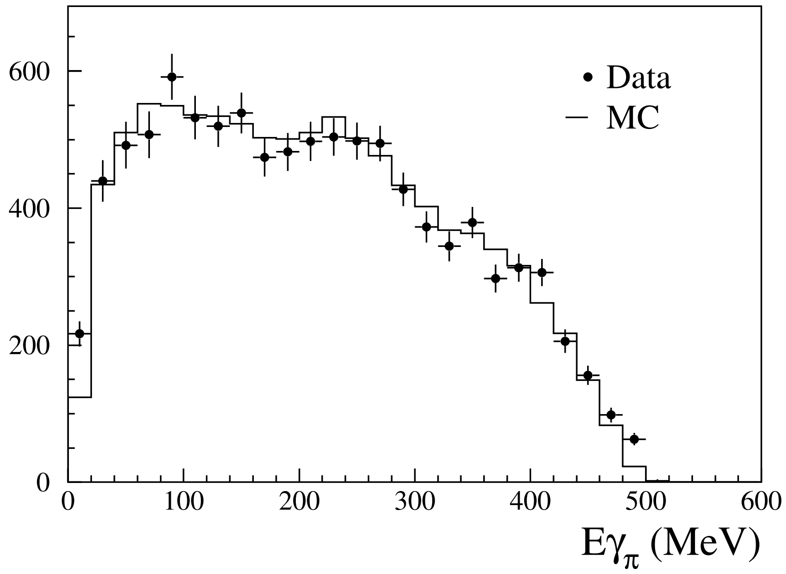

Figure 18: Data–MC comparison for $\phi \to \pi^0\pi^0\gamma$ events after background subtraction: energy of the photons produced by the two π^0's decay. Output of Fit2 is used.

Sample	P_1 (MeV)	P_2
DATA	1.15 ± 0.02	1.46 ± 0.01
MC	1.11 ± 0.01	1.56 ± 0.01

Table 4: Fit parameters for the π^0 mass resolution after Fit1.

where there is a $\sim 20\%$ discrepancy. The fits overimposed follow the parametrization

$$\sigma_\pi = \frac{P_1}{[E\ (\mathrm{GeV})]^{1/P_2}} \tag{7}$$

and give the parameters listed in Tab. 4.

The reasonable data–MC agreement of the pion mass resolution allows us to use MC parametrization also for the $M_{\pi\pi}$ resolution. In order to determine it we use only the events having the right photon assignement in the MC; in Fig. 22 the distribution of $M_{\pi\pi} - M_{\mathrm{true}}$ is shown and is consistent with a gaussian of $\sigma_M = 6$ MeV width.

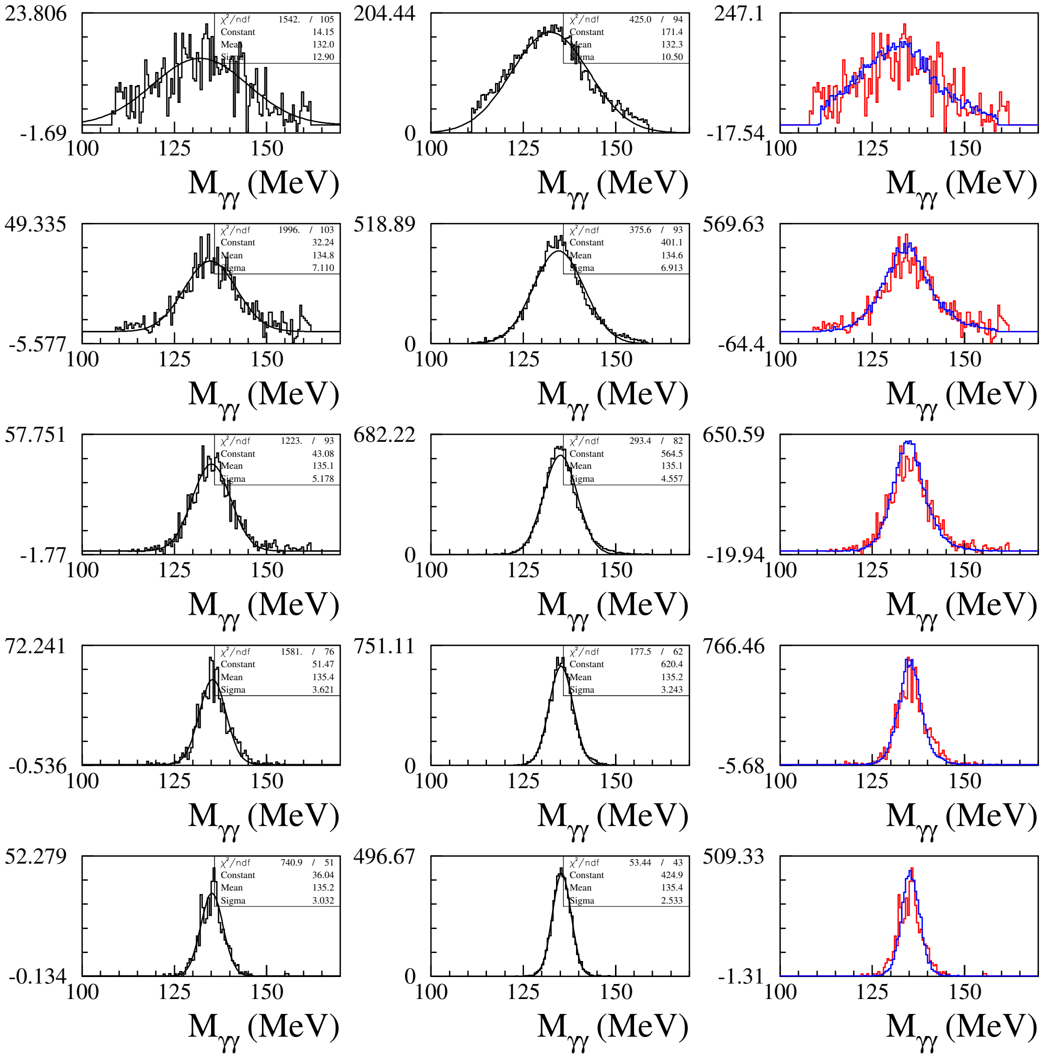

Figure 19: $M_{\gamma\gamma}$ distributions after Fit1 for different range of $E_{\min}$. From top to bottom: $0 \div 50$ MeV, $50 \div 100$ MeV, $100 \div 150$ MeV, $150 \div 200$ MeV and $200 \div 250$ MeV. The distributions displayed are: on the left the data, in the middle the MC ones and on the right the overpostion of the two (data in red, MC in blue).

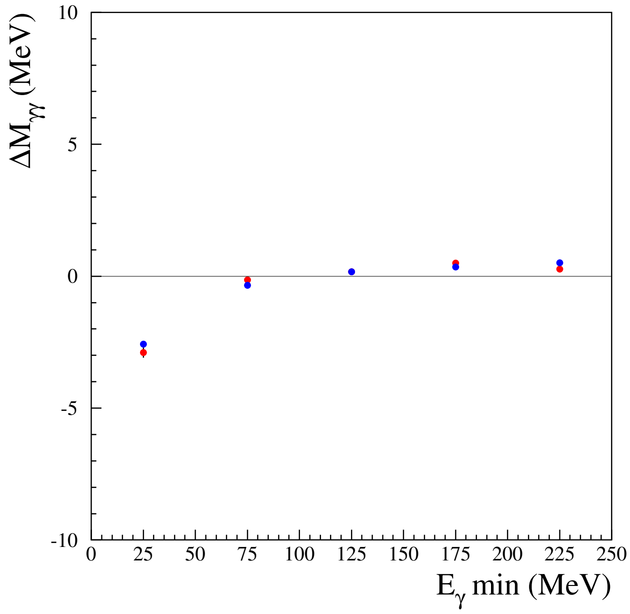

Figure 20: Average values of $M_{\gamma\gamma} - M_{\pi}$ as a function of $E_{\gamma\,\min}$. Red (blue) circles represents data (MC) results. Output variables of Fit1 are used.

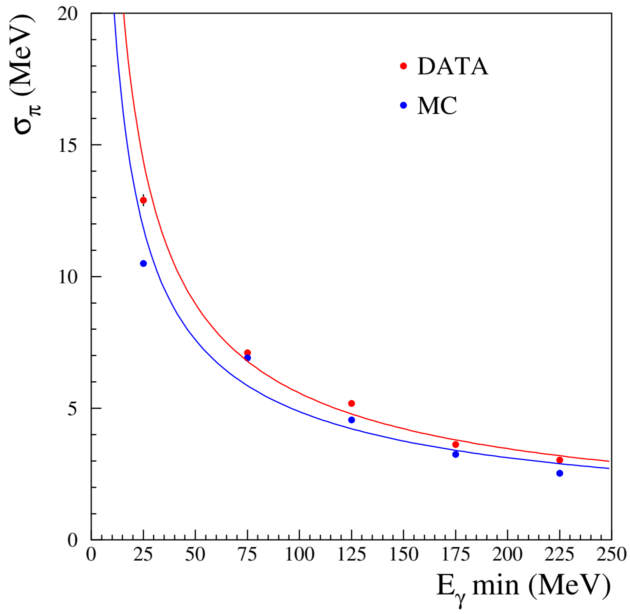

Figure 21: Fit1 π^0 mass resolution as a function of $E_{\min}$.

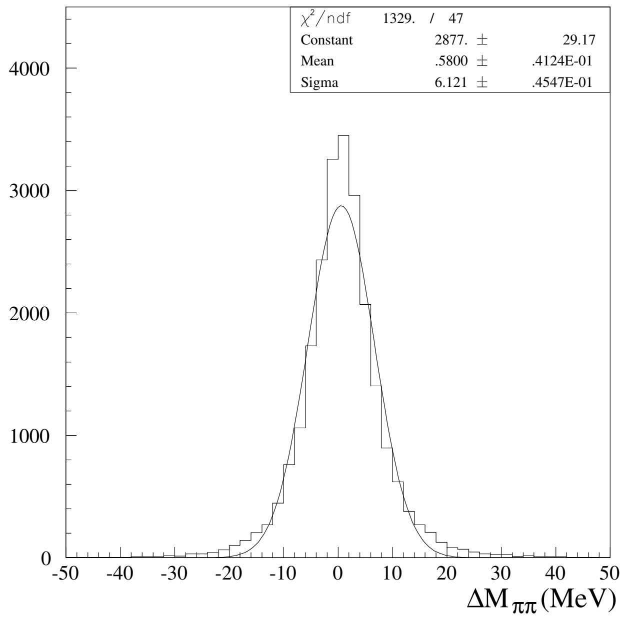

Figure 22: Distribution of $M_{\pi\pi} - M_{\rm true}$ for Montecarlo events with good photon assignment. Output of Fit2 is used.

The efficiency of good photon pairing has been studied by Montecarlo as a function of $M_{\rm true}$ (Fig. 23.top); the overall probability of wrong photon assignment, $\varepsilon_{\rm wp}$, is around 11%. The difference $\Delta M_{\pi\pi} = M_{\pi\pi} - M_{\rm true}$ for the events with bad pairing has the shape of Fig. 23.bottom-left and a behaviour as a function of $M_{\rm true}$ reported in Fig. 23.bottom-right. The $\Delta M_{\pi\pi}$ distributions are also shown for different $M_{\rm true}$ mass range in Fig. 24.

To measure the percentage of wrong pairing in the data the difference of the two lowest selection χ^2 in the event, $\Delta\chi^2_{\rm sel}$, is used. In Figs. 25.top the shape of this variable for good and bad pairing is shown; in the latter case the distribution is concentrated at low values of $\Delta\chi^2_{\rm sel}$. These templates are used to fit the data (Fig. 25.bottom), by minimizing the variable:

$$\chi^2 = \sum_i \frac{N^i_{\rm obs} - \alpha({\rm P1}\, N^i_{\rm bad} - {\rm P2}\, N^i_{\rm good})}{N^i_{\rm obs}} \tag{8}$$

where $N^i_{\rm obs}$, $N^i_{\rm bad}$ and $N^i_{\rm good}$ are the number of events for the three samples (data, correct pairing and wrong pairing respectively) in the i-th bin of $\Delta\chi^2_{\rm sel}$ distributions. The parameter $\alpha = \sum_i N^i_{\rm obs} / \sum_i (N^i_{\rm good} + N^i_{\rm bad})$ normalizes the MC entries to the number of

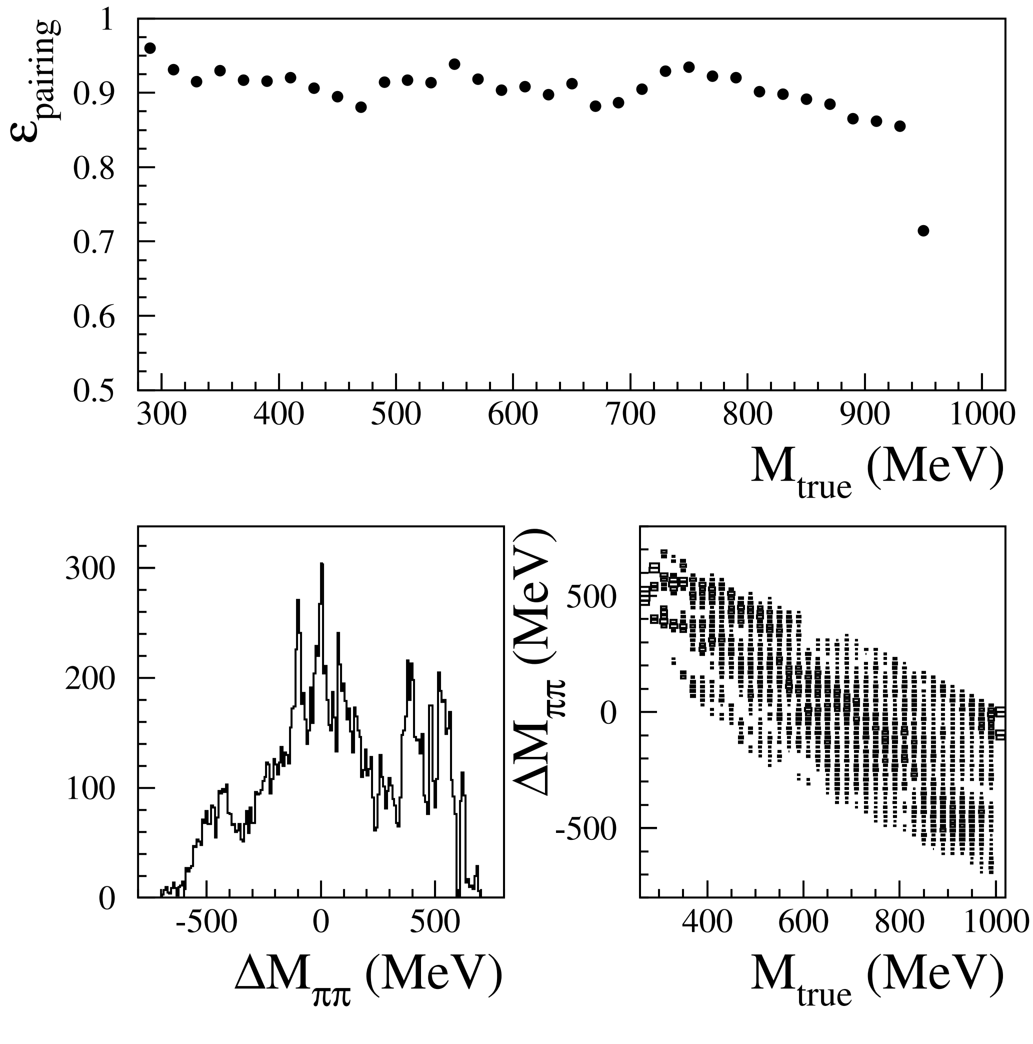

Figure 23: Efficiency of correct photon pairing vs M_{true} (top), $\Delta M_{\pi\pi}$ distribution for events with wrong photon pairing (bottom-left) and its behaviour as a function of M_{true} (bottom-right).

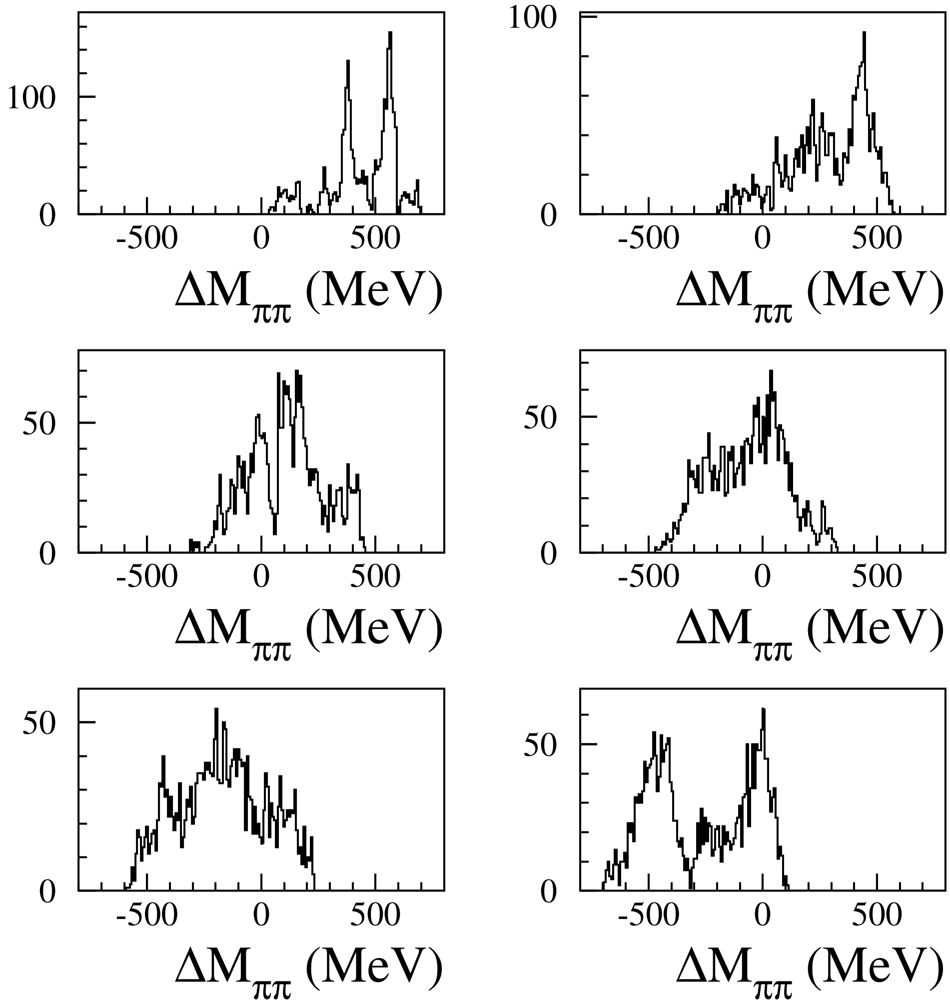

Figure 24: $\Delta M_{\pi\pi}$ distribution for events with wrong photon pairing for different $M_{\rm true}$ mass range: $300 \div 420$ MeV (top-left), $420 \div 540$ MeV (top-right), $540 \div 660$ MeV (middle-left), $660 \div 780$ MeV (middle-right), $780 \div 900$ MeV (bottom-left), $900 \div 1020$ MeV (bottom-right).

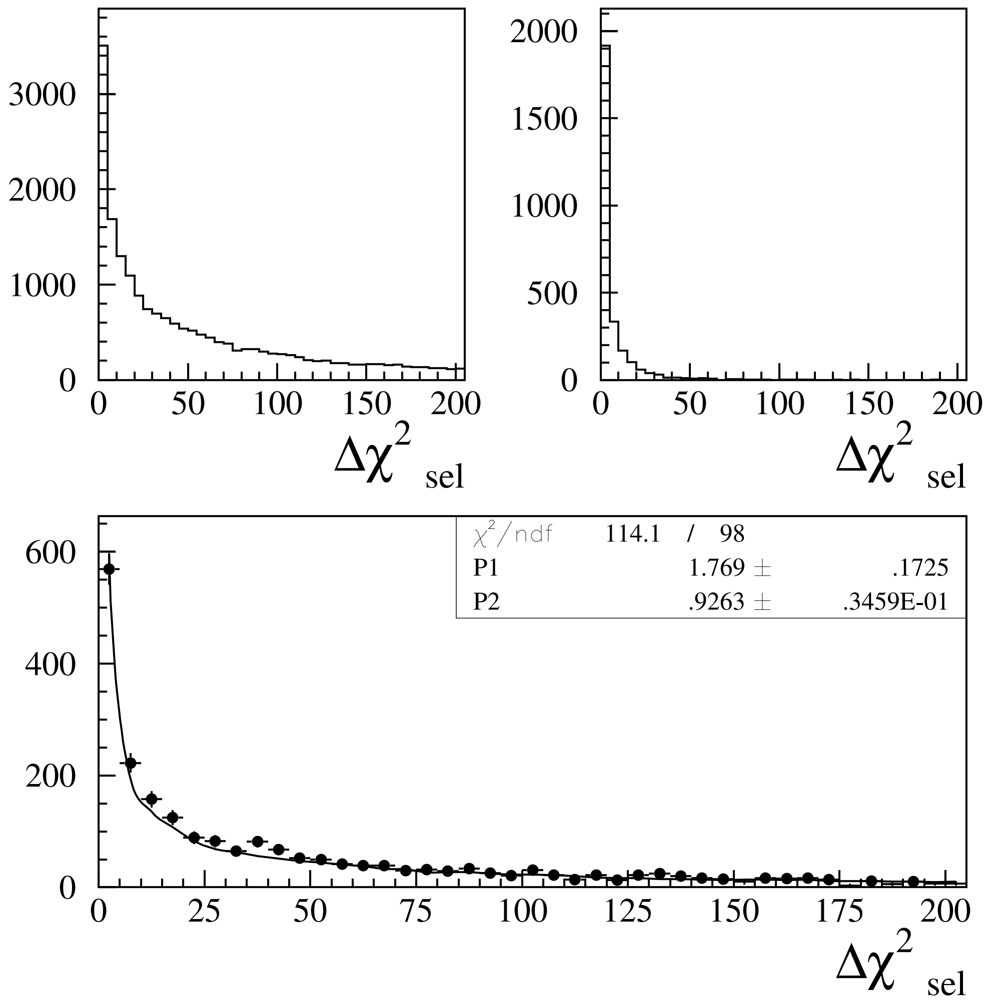

Figure 25: Montecarlo $\Delta\chi^2_{\rm sel}$ shapes for events with correct (top-left) and wrong (top-right) photon pairing. These two templates are used to fit the $\Delta\chi^2_{\rm sel}$ data distribution (bottom).

events in the data. A correction factor $\varepsilon_{\rm wp}(\text{data})/\varepsilon_{\rm wp}(\text{MC}) = (1.7 \pm 0.2)$ is found. One of the reasons for such a discrepancy could be the slightly different data–MC behaviour of the π^0 mass resolution and the usage of the average value for σ_π in the $\chi^2_{\rm sel}$. However, as it will be shown in Par. 4.6, this discrepancy is small enough not to influence our BR measurement.

A discrete convolution function, $\mathrm{G}(m_i, M_{\pi\pi})$, representing the probability for an event generated in the i-th bin of true mass (m) to be observed at reconstructed values of $M_{\pi\pi}$, has then been built. We used a theory (experiment) binning width of 5 MeV (20 MeV). The function $\mathrm{G}(m_i, M_{\pi\pi})$ is given by:

$$\mathrm{G}(m_i, M_{\pi\pi}) = \varepsilon_{\rm wp}(m_i) \cdot \mathrm{BADMAT}(m_i, M_{\pi\pi}) + (1 - \varepsilon_{\rm wp}(m_i)) \cdot \mathrm{GAUMAT}(m_i, M_{\pi\pi}) \quad (9)$$

where BADMAT and GAUMAT are the matrices describing the probability of bad pairing and gaussian smearing.

4.5 Systematics on event selection

The systematic error on counting of $\pi\pi\gamma$ events is obtained by summing in quadrature the following effects.

1. **Trigger and data streaming losses**
   As explained in Par. 3, all losses due to data streaming are negligible. Although we found a loss of $(3.9 \pm 0.8) \cdot 10^{-3}$ due to the cosmic veto, we did not apply it and just add half of this correction (0.2%) to the global systematic error.

2. **Photons counting**
   The systematic error on the selection efficiency of five prompt photons is related to the simulation accuracy in describing the clustering, which means single cluster efficiency, probability of generating a fragment, probability of being merged and external accidental contamination. As explained in Par. 2, we have inserted in the MC the cutoff introduced by the ADC, TDC thresholds to get a more realistic simulation of the efficiency. Moreover, we have also added in the simulation the contamination of accidental clusters due to machine background. In order to assign a systematic error on the exclusive counting of photons in acceptance we have used a clean sample of $\phi \to \eta\gamma \to \pi^0\pi^0\pi^0\gamma$ events, performing the following tests [11]:

(a) we have used in the MC three different parametrizations for the threshold cutoff, obtaining a relative systematic error of $(+0.8, -1.5)\%$.

(b) the production cross-section for this process, $\sigma_{\eta 7}$, has been measured using exclusively 6 and 7 reconstructed clusters or at least 6 reconstructed clusters. With respect to the measurement with 7 clusters we have a relative variation of $\sigma_{\eta 7}$ of $+1.4\%$ ($+0.2\%$) using 6 or at least 6 clusters. This shows how well the simulation reproduce fragments, geometrical acceptance and merging.

(c) an higher threshold (20 MeV) has been used. The $\sigma_{\eta 7}$ evaluated in this way shows a relative variation of -0.6% from the one where a standard 7 MeV threshold is used. This estimates the systematic errors connected to the energy dependence of $\varepsilon_{\rm clu}$, to any possible effect due to energy scale and to the MC description of the accidentals.

Combining these three tests together we get a relative error on the efficiency of counting 7 γ's which is of $\pm 1.4\%$. It is not simple to scaling it down to 5 clusters; if we assume that the MC correctly describes the geometrical acceptance, a reduction factor 5/7 can be guessed reducing the total relative error to 1.0%.

3. **Background**

   For the background, the systematic error is related to the KLOE measurement of these processes. This leads to a $\pm 1.3\%$ relative error on the total event counting.

4. **Analysis cuts**

   As it was shown in Figs 17, the expected angular distributions are well reproduced by our candidates but we cannot exclude a small error on the background contamination. Indeed, the background error evaluated above do not take into account the tails in the QED processes and the possibility of an enhancement in $\varepsilon_{\rm wp}$ for the considered backgrounds. In order to test these residual unknown effects we have varied of $\pm 1^\circ$, $\pm 1\sigma_\pi$ the $\theta_{\rm min}$, $\Delta M_{\gamma\gamma}$ cuts respectively. This contributes of 2.0% to the total relative error.

4.6 BR evaluation

The reconstructed mass spectrum of Fig. 17, $S_{\rm rec}(M_{\pi\pi})$, has been fitted by folding the theoretical function, $f(m)$ [10], with analysis efficiencies, experimental resolutions and

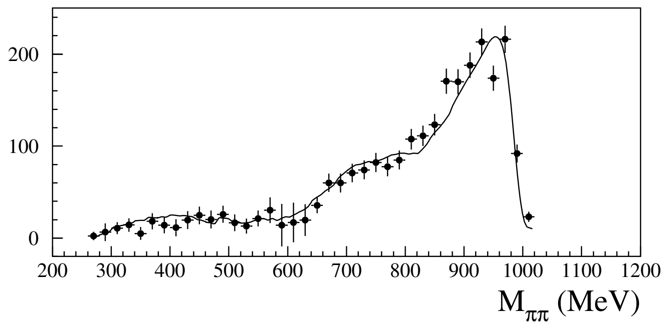

Figure 26: Fit to the $M_{\pi\pi}$ spectrum.

reconstruction effects described by the discrete convolution function $G(m_i, M_{\pi\pi})$ as:

$$S_{\rm rec}(M_{\pi\pi}) = \sigma(\phi)\, L_{\rm int}\, \sum_i \left[\, f(m_i)\, \Delta m\, {\rm G}(m_i, M_{\pi\pi}) \cdot \varepsilon_{\pi\pi\gamma}(m_i)\right], \tag{10}$$

where $\sigma(\phi)$ is the ϕ production cross section and Δm represents the mass binning used for the theory. The result of the fit, described in more detail in Ref. [10], is shown in Fig. 26.

In order to obtain the normal differential decay rate, $d{\rm BR}/dm = \frac{d\Gamma/dm}{1/\Gamma_\phi}$, the fit results are used to unfold $S_{\rm rec}(M_{\pi\pi})$, using for each reconstructed mass bin the ratio between the theoretical and the smeared function, $SF(M_{\pi\pi})$, shown in Fig. 27:

$$\frac{d{\rm BR}}{dm} = \frac{S_{\rm rec}(M_{\pi\pi})}{SF(M_{\pi\pi})}\, \frac{1}{\Delta M_{\pi\pi}\, L_{\rm int}\, \sigma(\phi)} \tag{11}$$

For the BR normalization, the ϕ production cross section ($\sigma(\phi)$) measurement coming from the $\phi \to \eta\gamma \to \gamma\gamma\gamma$ decay in the same sample is used [11]. The $d{\rm BR}/dm$ as a function of $M_{\pi\pi}$ is listed in Tab. 5 and shown in Fig. 28; the overall total uncertainty is given by the quadrature of the relative errors summarized in Tab. 6. The resulting shape is in good agreement with the one obtained by the SND experiment [2] (Fig. 28). Integrating over the whole mass range we obtain

$${\rm BR}(\phi \to \pi^0\pi^0\gamma) = (1.09 \pm 0.03_{\rm stat} \pm 0.03_{\rm syst} \pm 0.04_{\rm norm}) \cdot 10^{-4}, \tag{12}$$

while considering the f_0 dominated region, above 700 MeV:

$${\rm BR}(\phi \to \pi^0\pi^0\gamma\,;\, m > 700 \text{ MeV}) = (0.96 \pm 0.02_{\rm stat} \pm 0.02_{\rm syst} \pm 0.04_{\rm norm}) \cdot 10^{-4}. \tag{13}$$

In order to evaluate the effect of the knowledge on the convolution function, we have varied $\varepsilon_{\rm wp}$ of $\pm 1\sigma$ and σ_M of ± 1 MeV in the fit procedure, observing a negligible variation in the BR value.

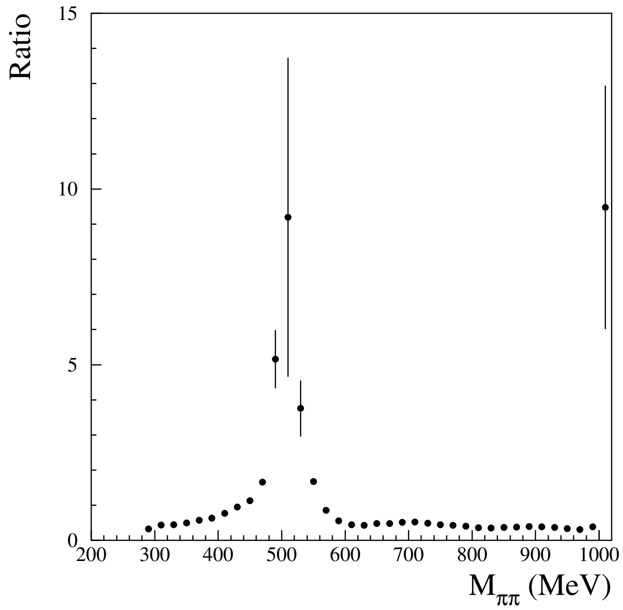

Figure 27: The ratio $S_{\rm rec}(M_{\pi\pi})/SF(M_{\pi\pi})$ used to unfold the data.

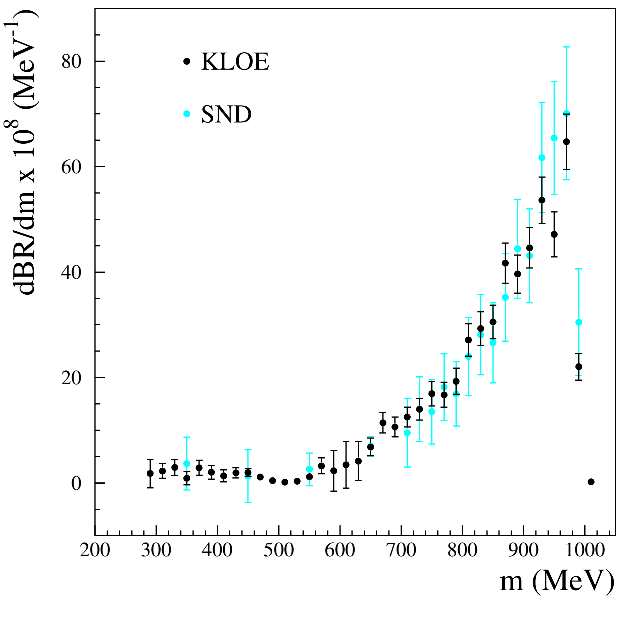

Figure 28: dBR$/dm$ as a function of m. The SND shape is also displayed.

m (MeV)	$\frac{d\text{BR}}{dm}$ ($10^8\,\text{MeV}^{-1}$)	m (MeV)	$\frac{d\text{BR}}{dm}$ ($10^8\,\text{MeV}^{-1}$)
290	2.0 ± 2.9	670	11.2 ± 1.9
310	2.2 ± 1.4	690	11.0 ± 1.9
330	3.0 ± 1.5	710	12.5 ± 1.9
350	0.9 ± 1.3	730	14.0 ± 2.0
370	2.9 ± 1.4	750	17.3 ± 2.3
390	2.2 ± 1.3	770	17.0 ± 2.4
410	1.4 ± 1.1	790	19.4 ± 2.5
430	1.8 ± 1.0	810	27.4 ± 3.1
450	1.9 ± 0.8	830	29.2 ± 3.2
470	1.1 ± 0.5	850	30.6 ± 3.2
490	0.5 ± 0.2	870	41.7 ± 3.8
510	0.2 ± 0.1	890	39.6 ± 3.6
530	0.3 ± 0.2	910	44.6 ± 3.8
550	1.3 ± 0.5	930	53.6 ± 4.4
570	3.3 ± 1.5	950	47.2 ± 4.3
590	2.1 ± 3.6	970	64.7 ± 5.3
610	3.7 ± 4.7	990	22.0 ± 2.5
630	4.2 ± 3.7	1010	0.2 ± 0.1
650	7.0 ± 1.7		

Table 5: Differential BR for $\phi \to \pi^0\pi^0\gamma$. The errors listed are the total uncertainties.

Source	Relative error
Statistics	2.5%
Background	1.3%
Events counting	2.3%
Normalization	3.7%

Table 6: Uncertainties on BR($\phi \to \pi^0\pi^0\gamma$).

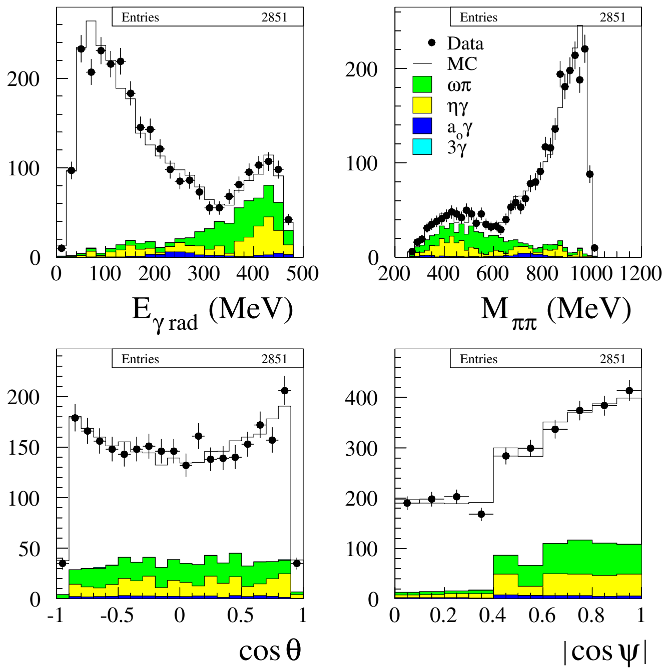

Figure 29: Data–MC comparison for $\phi \to \pi^0\pi^0\gamma$ events analyzed with ANA1: energy of the radiative photon (up-left), $\pi^0\pi^0$ invariant mass (up-right), polar angle (bottom-left) and $|\cos\psi|$ distribution (bottom-right) after analysis cuts. The expected background contribution is displayed in colors.

Since the MC shape of the $\pi^0\pi^0$ invariant mass reproduces the data, the total BR can also be calculated, in a simpler way, using the number of $\pi\pi\gamma$ candidates ($N_{\pi\pi\gamma}$) and the overall analysis efficiency ($\varepsilon_{\pi\pi\gamma} = 41.6\%$). We obtain

$$\mathrm{BR}(\phi \to \pi^0\pi^0\gamma) = \frac{N_{\pi\pi\gamma}}{L_{\mathrm{int}} \cdot \sigma(\phi) \cdot \varepsilon(\pi\pi\gamma)} = (1.08 \pm 0.03_{\mathrm{stat}} \pm 0.03_{\mathrm{syst}} \pm 0.04_{\mathrm{norm}}) \cdot 10^{-4}, \quad (14)$$

which is in full agreement with the previous result.

4.7 Comparison with OLDANA

In order to check the stability of the $\mathrm{BR}(\phi \to \pi^0\pi^0\gamma)$ measurement, the analysis of Sample A has been repeated with the OLDANA cuts. The result, obtained using the overall analysis efficiency as in Eq. (14), is the same of NEWANA:

$$\mathrm{BR}(\phi \to \pi^0\pi^0\gamma\,;\,\mathrm{OLDANA}) = (1.08 \pm 0.03_{\mathrm{stat}} \pm 0.03_{\mathrm{syst}} \pm 0.04_{\mathrm{norm}}) \cdot 10^{-4} \quad (15)$$

The data–MC agreement is excellent also in this case (Fig. 29).

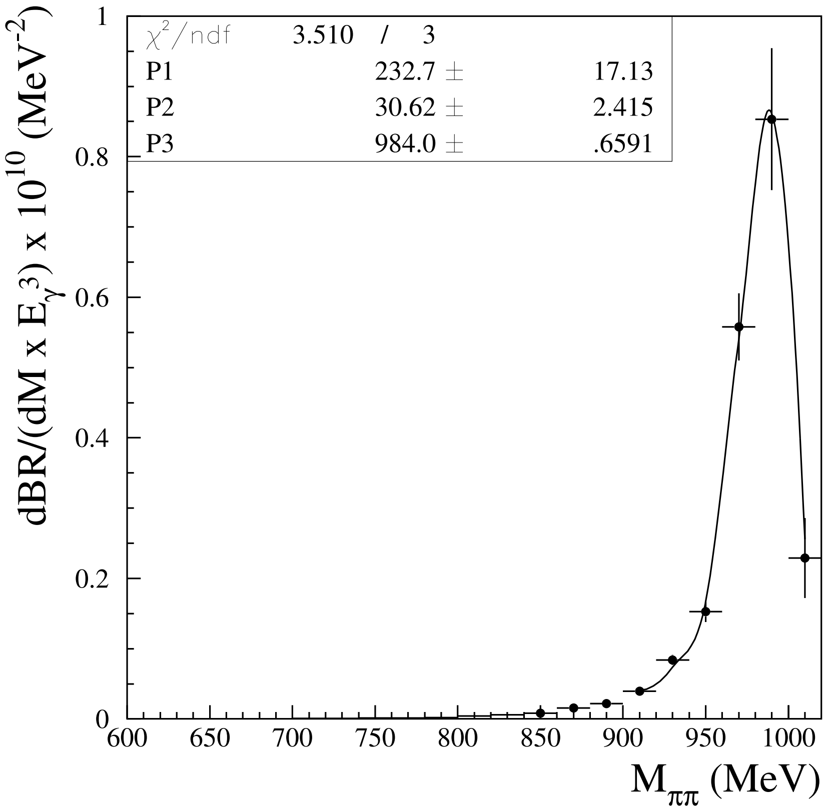

Figure 30: $d\text{BR}/dm$ after the E_γ^3 correction.

4.8 Correcting for the probability of the radiative transition

As it is explained more in detail in Ref. [10], the $d\Gamma/dm$ is given by:

$$\frac{d\Gamma(\phi \to S\gamma \to \pi^0\pi^0\gamma)}{dm} = \frac{2m^2}{\pi}\frac{\Gamma(\phi \to S\gamma)\,\Gamma(S \to \pi^0\pi^0)}{|D_S|^2} \tag{16}$$

In a phenomenological way, the radiative transition $\phi \to S\gamma$ is proportional to E_γ^3. As an exercize, we plot in Fig. 30 the distribution of $\frac{d\text{BR}}{dm}/E_\gamma^3$. As it can be observed all the long tail disappears and the distribution is consistent with a simple Breit-Wigner of 30 MeV width.

Acknowledgements

It is a pleasure to thank the people that helped us in this work. First of all, we are in debt with R. Escribano that has discussed with us the interpretation of the theoretical framework. We want also to thank C. Bloise for the help in testing the $e^+e^- \to \omega\pi^0$ simulation. We finally thank our referees, A. Di Domenico and G. De Zorzi, to have followed closely the latest development of this analysis.

References

[1] M.N. Achasov *et al.*, Phys. Lett. B 440 (1998) 442.

[2] M. N. Achasov *et al.*, Phys. Lett. B 485 (2000) 349.

[3] R.R. Akhmetshin *et al.*, Phys. Lett. B 462 (1999) 380.

[4] N.A. Törnqvist, Phys. Rev. Lett. 49 (1982) 624.

[5] R.L. Jaffe, Phys. Rev. D 15 (1997) 267.

[6] J. Weinstein and N. Isgur, Phys. Rev. Lett. 48 (1982) 659.

[7] R.R. Akhmetshin *et al.*, Phys. Lett. B 462 (1999) 371.

[8] F. Ambrosino *et al.*, KLOE Memo 212 (2000).

[9] S. Giovannella S. Miscetti, KLOE Memo 244 (2001).

[10] C. Bini *et al.*, KLOE Memo 269 (2002).

[11] S. Giovannella S. Miscetti, KLOE Note 177 (2002).

[12] S. Miscetti and T. Spadaro, KLOE Memo 251 (2001).

[13] S. Miscetti, KLOE Memo in writing

[14] M. Adinolfi *et al.*, Nucl. Inst. and Meth. A 461 (2001) 465.

[15] C. Bini *et al.*, KLOE Memo 126 (1997).
A. Menicucci G. Finocchiaro, KLOE Memo 204 (1999).
A. Menicucci G. Finocchiaro, KLOE Memo 205 (1999).

[16] C. Bini P. Gauzzi, KLOE Memo 171 (1998).

[17] C. Bloise C. Forti, KLOE Memo 241 (2001).

[18] A. Denig, KLOE Phisics Workshop at la Biodola, 23th-25th May 2001 (*http://www.lnf.infn.it/kloe/private/biodola/denig.pdf*) and private communication.

[19] P. Gauzzi, KLOE Memo in writing.

[20] M. N. Achasov *et al.*, Nucl. Phys. B 569 (2000), 158-182.